Interaction between a Rising Bubble and a Stationary Droplet Immersed in a Liquid Pool using a Ternary Conservative Phase-Field Lattice Boltzmann Method

Chunheng Zhao and Taehun Lee*

Department of Mechanical Engineering,

City College of New York, New York 10031, USA

(Dated: February 7, 2023)

Abstract

When a stationary bubble and a stationary droplet immersed in a liquid pool are brought into contact, they form a bubble-droplet aggregate. Its equilibrium morphology and stability largely depend on the combination of different components' surface tensions, known as the "spreading factor." In this study, we look at the interaction between a rising bubble and a stationary droplet to better understand the dynamics of coalescence and rising and morphological changes for the bubble-droplet aggregate. A systematic study is conducted on the interaction processes with various bubble sizes and spreading factors in 2 dimensions. The current simulation framework consists of the ternary conservative phase-field Lattice Boltzmann method (LBM) for interface tracking and the velocity-pressure LBM for hydrodynamics, which is validated by benchmark cases such as the liquid lens and parasitic currents around a static droplet with several popular surface tension formulations. We further test our LBM for the morphology changes of two droplets initially in contact with various spreading factors and depict the final morphologies in a phase diagram. The separated, partially engulfed, and completely engulfed morphologies can be replicated by systematically altering the sign of the spreading factors. The rising bubble and stationary droplet interaction are simulated based on the final morphologies obtained under stationary conditions by imposing an imaginary buoyancy force on the rising bubble. The results indicate that the bubble-droplet aggregate with double emulsion morphology can minimize the distortion of the bubble-droplet aggregate and achieve a greater terminal velocity than the aggregate with partially engulfed morphology.

---

* thlee@ccny.cuny.edu

I. INTRODUCTION

The rising bubble and droplet interaction is one of the common phenomena found in gas flotation, water cleanup and oil extraction [1–3]. The entire interaction can be divided into the following three parts: the bubble-rising process, the bubble droplet interaction process, and the aggregate-rising process. These processes have been studied to develop an optimal system by experiments and simulations for decades [4–6]. When small bubbles are injected into a liquid pool with immiscible oil droplets, bubbles with a lower density rapidly rise due to buoyancy. Numerous rising bubbles touch oil droplets, and the surface tension between the bubbles and droplets initiates the bubble-droplet interaction. Depending on spreading factors derived from surface tensions among three different components, three distinct bubble-droplet morphologies are expected: (1) separated bubble-droplet morphology; (2) partially engulfed morphology; and (3) completely engulfed morphology [7]. The stability of the bubble-droplet aggregate depends highly on the surface tension between the aggregate and the liquid pool. If the surface tension is strong enough, the aggregate will maintain its shape and continue to rise. On the contrary, a weak surface tension will induce further deformation as the aggregate rises, and the velocity of the aggregate will decrease quickly, which may lead to the breakup of the aggregate.

A simple interaction of bubble and droplet occurs in a ternary flow that includes a gas bubble, and an oil droplet in a liquid pool. The interaction prompts complex interface deformation and morphological change which is challenging to be tracked by any simulation methods. Among several interface tracking methods, the diffuse interface method utilizes the free energy variation, which results in a thermodynamically consistent system [8, 9]. Both the Cahn-Hilliard (C-H) equation and the Allen-Cahn (A-C) equation [10, 11] have been applied to solve the phase transformation as diffuse interface methods. Compared to the A-C equation, the C-H equation keeps the mass conserved by a conservative formulation, hence, it has been widely utilized in the multi-phase flow simulation [12–15]. However, the loss of mass and density shift are still observed when it is used to model a small radius bubble or droplet due to the implicit curvature-driven velocity [9, 16–18]. Thus, many efforts have been made to modify the A-C equation in order to create a formulation that is both efficient and conservative. Based on the phase-field model conducted by R. Folch [19] and the sharp interface tracking method investigated by Sun and Beckermann [16],

Chiu proposed the conservative phase-field method [20]. The essential idea behind this method is to remain the conservation by removing the curvature-driven velocity from the A-C equation and moving the diffusion terms into the divergence operator. This modification offers a remarkable improvement in mass conservation compared to the C-H equation [9]. Furthermore, compared to the C-H equation, where we have to solve the fourth-order partial differential equation, the conservative phase-field equation only solves a second-order partial differential equation. This feature omits the higher-order derivative calculation, which makes the numerical computation considerably easier. By adding a Lagrange multiplier, the model is then optimized to solve the multi-component system [21–24].

According to [6], the equilibrium morphology and the aggregate stability mostly depend on the surface tension and the combination of different components' spreading factors. Since the surface tensions are explicitly given naturally, how to model the surface force can then be crucial during the simulation. As far as we are concerned, three well-known surface force forms in this article are presented: (1) continuum surface force (CSF) formulation [12, 25]; (2) potential form formulation [26]; (3) stress form formulation [27]. Unlike the C-H equation, the free energy of the conservative phase-field equation is not yet complete due to the subtraction of the curvature-driven velocity. In this instance, we claim that the potential formulation, which is mostly derived from an energy perspective, combined with the conservative phase-field equation will not be able to reduce parasitic currents' intensity as effectively as it did previously[28]. We conduct the simulations based on the Lattice Boltzmann method (LBM). LBM has been widely applied to solve the Navier-Stokes equation for incompressible flow [14, 29, 30] and shown as an effective method to solve the multi-phase flow problem by pseudo-potential LBM [31] and phase-field LBM [13, 22, 32, 33]. Previously, high densities and viscosities were encountered when the LBM was utilized to model the multi-phase flow. To increase the system's instability, Lee introduces the multi-step collision and mixed difference method [13]. For incompressible two-phase flow, Inamuro suggests the free energy LBM [34]. Zu and He propose the velocity-based LBM to solve the high-density ratio problems [35]. It is noted that the previous model cannot entirely recover the continuity equation, and to improve this, a new velocity-pressure based LBM is proposed to deal with the problem of large ratio parameters [9]. In this method, the coupled continuity equation and pressure evolution equation can be recovered through Chapman Enskog analysis. Besides, this approach greatly decreases the requirement for a

thick interface thickness which makes it easy to obtain a sharp interface limit [13].

In this study, we combine the conservative phase-field LBM with the velocity-pressure-based LBM. The following section goes over the derivation specifics for each LBM. In terms of the simulation, the benchmark problems, including parasitic currents and liquid lens are conducted to validate the conservative character and the accuracy of the recent model. We further investigate the morphology changing problem and post the results in a diagram. Then, the dynamics of a single rising bubble are investigated, and the convergence test is conducted using the present method. Finally, we present the simulation of the rising bubble and droplet interaction. The stability and the terminal velocity of different morphologies are tested under different Bond numbers.

II.   CONSERVATIVE PHASE-FIELD LATTICE BOLTZMANN EQUATION

A.   Conservative Phase-field Equation

The two-component conservative phase-field equation can be derived either by the free energy approach from the Allen Cahn equation [23] or by the velocity-based approach from the generic interface advection equation [16]. In the following section, the derivation based on the velocity-based approach is described [21].

1.   Conservative Phase-field Equation for Two-component Flows

Consider the following interface advection equation for a two-phase flow system:

$$\frac{\partial \phi}{\partial t} + \boldsymbol{u} \cdot \nabla \phi = 0, \tag{1}$$

where the order parameter ϕ with the constraint $0 \leq \phi \leq 1$ is used to denote different fluid's regions. The flow velocity is represented by $\boldsymbol{u}$ which can be divided into a normal velocity $\boldsymbol{u}_n$ and an external advection velocity $\boldsymbol{u}_e$ as follow:

$$\boldsymbol{u} = \boldsymbol{u}_n + \boldsymbol{u}_e. \tag{2}$$

The normal velocity $\boldsymbol{u}_n$ can be further decomposed as:

$$\boldsymbol{u}_n = -M\kappa\boldsymbol{n}, \tag{3}$$

where M is the mobility, which is a pure calculation parameter; κ denotes the interface curvature; and $\boldsymbol{n}$ represents the unit normal vector. $\boldsymbol{n}$ and κ can be expressed as a function of the order parameter ϕ:

$$\boldsymbol{n} = \frac{\nabla\phi}{|\nabla\phi|}, \tag{4}$$

$$\kappa = \nabla \cdot \boldsymbol{n} = \frac{1}{|\nabla\phi|}\left[\nabla^2\phi - \frac{\nabla\phi \cdot \nabla|\nabla\phi|}{|\nabla\phi|}\right]. \tag{5}$$

Substituting Eq. (4) and Eq. (5) into Eq. (1), we can reformulated Eq. (1) as:

$$\frac{\partial\phi}{\partial t} + \boldsymbol{u}_e \cdot \nabla\phi = M\kappa|\nabla\phi| = M\left[\nabla^2\phi - \frac{\nabla\phi \cdot \nabla|\nabla\phi|}{|\nabla\phi|}\right] = M\left[\nabla^2\phi - \boldsymbol{n} \cdot \nabla|\nabla\phi|\right]. \tag{6}$$

It is noteworthy that Eq. (6) is not in a conservative form and thus will induce a mass conservation error. To overcome this, Folch *et al.* [19] proposed to explicitly remove the curvature driven part from Eq. (6), which leads to:

$$\frac{\partial\phi}{\partial t} + \boldsymbol{u}_e \cdot \nabla\phi = M\left[\nabla^2\phi - \boldsymbol{n} \cdot \nabla|\nabla\phi| - |\nabla\phi|\nabla \cdot \boldsymbol{n}\right] \approx M\left[\nabla^2\phi - \nabla \cdot (|\nabla\phi^{eq}|\boldsymbol{n})\right]. \tag{7}$$

Here ϕ^{eq} is the equilibrium profile of the order parameter for a planar interface, which is represented by a hyperbolic tangent function as follows:

$$\phi^{eq} = \frac{1}{2}\left[1 + \tanh\left(\frac{2z}{\delta}\right)\right], \tag{8}$$

where z is the normal distance between a local point and the interface with the interface thickness being adjusted by δ. Eq. (8) results in:

$$|\nabla\phi^{eq}| = \frac{\partial\phi^{eq}}{\partial\boldsymbol{n}} = \frac{4\phi(1-\phi)}{\delta}. \tag{9}$$

Once Eq. (9) is substituted into Eq. (7) and the continuity condition $\nabla \cdot \boldsymbol{u}_e = 0$ is imposed,

we arrive at the conservative phase-field equation for two-phase flow:

$$\frac{\partial \phi}{\partial t} + \nabla \cdot (\phi \boldsymbol{u_e}) = \nabla \cdot M \left[\nabla \phi - \frac{4\phi(1-\phi)/\delta}{|\nabla \phi|} \nabla \phi \right]. \tag{10}$$

2.   Conservative Phase-Field Equation for Multi-component Flows

The following is how we arrive at the conservative phase-field equation for multi-component flows. Based on the two-phase flow model, we further introduce the Lagrange multiplier ψ_i [36] to the original two-component flow model to satisfy the constraint of the multi-component systems. The order parameter of the ith component in the n-component flow is represented by ϕ_i in the following derivation. We start with:

$$\frac{\partial \phi_i}{\partial t} + \nabla \cdot (\phi_i \boldsymbol{u}) = \nabla \cdot M \left(\nabla \phi_i - \frac{4\phi_i(1-\phi_i)/\delta}{|\nabla \phi_i|} \nabla \phi_i + \psi_i \right). \tag{11}$$

In order to determine the Lagrange multiplier ψ_i, we first consider a system at the equilibrium, for which the left-hand side of Eq. (11) disappears. The summation of the phase-field equations can be calculated as:

$$\sum_{i=1}^{n} \psi_i = \sum_{i=1}^{n} \frac{4\phi_i(1-\phi_i)/\delta}{|\nabla \phi_i|} \nabla \phi_i. \tag{12}$$

Following the method of the derivation of this Lagrange multiplier proposed by Kim [37], we assume the factor before the sum calculus as:

$$\psi_i = \frac{\phi_i^2}{\sum_{j=1}^{n} \phi_j^2} \sum_{j=1}^{n} \frac{4\phi_j(1-\phi_j)/\delta}{|\nabla \phi_j|} \nabla \phi_j. \tag{13}$$

Finally, the conservative phase-field equation for the multi-component flow is derived as:

$$\frac{\partial \phi_i}{\partial t} + \nabla \cdot (\phi_i \boldsymbol{u}) = \nabla \cdot M \left(\nabla \phi_i - \frac{4\phi_i(1-\phi_i)/\delta}{|\nabla \phi_i|} \nabla \phi_i + \frac{\phi_i^2}{\sum_{j=1}^{n} \phi_j^2} \sum_{j} \frac{4\phi_j(1-\phi_j)/\delta}{|\nabla \phi_j|} \nabla \phi_j \right).$$
$$\tag{14}$$

6

B. Formulations for Surface Tension Force

The momentum equation can be expressed as follows

$$\frac{\partial \boldsymbol{u}}{\partial t} + \nabla \cdot (\boldsymbol{u}\boldsymbol{u}) = -\frac{1}{\rho}\nabla p + \frac{1}{\rho}\nabla \cdot \eta \left(\nabla \boldsymbol{u} + (\nabla \boldsymbol{u})^T\right) + \frac{1}{\rho}\boldsymbol{F}_s + \frac{1}{\rho}\boldsymbol{F}_b, \tag{15}$$

where ρ and η represent the density and dynamic viscosity of a mixture. In Eq. (15), p is the dynamic pressure, $\boldsymbol{F}_s$ is the surface tension force, and $\boldsymbol{F}_b$ is the body force. We briefly list and compare the following formulations of surface tension force for two-phase flow

$$\boldsymbol{F}_{s1} = -\frac{3\sigma\delta}{2}\nabla \cdot \left(\frac{\nabla\phi}{|\nabla\phi|}\right)|\nabla\phi|^2\frac{\nabla\phi}{|\nabla\phi|}, \tag{16}$$

$$\boldsymbol{F}_{s2} = \mu\nabla\phi, \tag{17}$$

$$\boldsymbol{F}_{s3} = \frac{3\sigma\delta}{2}\nabla \cdot \left(|\nabla\phi|^2 I - \nabla\phi \otimes \nabla\phi\right). \tag{18}$$

Here σ represents the surface energy between two fluids. In Eq. (17), μ denotes the chemical potential that can be expressed as $\mu = \mu_0 - \epsilon\nabla^2\phi$, and $\mu_0 = \partial E_0/\partial\phi$ where $E_0 = \beta\phi^2(\phi-1)^2$ is the bulk energy. β is a constant that can be calculated from $\beta = 8\epsilon/\delta^2$ and related to the surface tension $\sigma = \sqrt{2\epsilon\beta}/6$.

Among three formulas, $\boldsymbol{F}_{s1}$ is proposed by Brackbill [25] as the continuum surface force (CSF). This model, as shown in Eq. 16, calculates the curvature by an explicit derivative of the order parameter, for which the performance highly depends on the derivative calculation. $\boldsymbol{F}_{s2}$ is the potential form formulation [8, 26]. $\boldsymbol{F}_{s3}$, the stress form formulation, is proposed by Lafaurie [27] which is the only formulation that conserves the momentum by the divergence operator. The potential form of surface tension force is mostly applied in LBM coupled with the C-H equation to decrease the parasitic currents' intensity by balancing the thermodynamic pressure [28, 38]. It is known that the phase-field equations, including the C-H equation and the A-C equation, could be derived from the free energy approach. However, we should notice that, compared to the original A-C equation, the conservative phase-field equation subtracts the curvature-driven term $\kappa|\nabla\phi|$ from the chemical potential. In this case, we argue that it is not consistent to calculate the surface tension force by the potential form formulation. Whereas, the CSF formulation provides an explicit curvature term and makes up the consistency.

C. Lattice Boltzmann equations

Through the above derivations, the governing equations for the ternary flow can be expressed as the pressure evolution equation, the velocity equation, and the conservative phase-field equations:

$$\frac{\partial \bar{p}}{\partial t} + \boldsymbol{u} \cdot \nabla \bar{p} + c_s^2 \nabla \cdot \boldsymbol{u} = 0, \tag{19}$$

$$\frac{\partial \boldsymbol{u}}{\partial t} + \nabla \cdot (\boldsymbol{u}\boldsymbol{u}) = -\frac{1}{\rho}\nabla P + \frac{1}{\rho}\nabla \cdot \eta \left(\nabla \boldsymbol{u} + (\nabla \boldsymbol{u})^T\right) + \frac{1}{\rho}\boldsymbol{F}_s + \frac{1}{\rho}\boldsymbol{F}_b, \tag{20}$$

$$\frac{\partial \phi_i}{\partial t} + \nabla \cdot (\phi_i \boldsymbol{u}) = \nabla \cdot M \left(\nabla \phi_i - \frac{4}{\delta}\frac{\nabla \phi_i}{|\nabla \phi_i|}\phi_i(1-\phi_i) + \frac{\phi_i^2}{\sum_{j=1}^3 \phi_j^2}\sum_{j=1}^3 \frac{4}{\delta}\frac{\nabla \phi_j}{|\nabla \phi_j|}\phi_j(1-\phi_j)\right). \tag{21}$$

In ternary flow, we normally solve two equations to calculate ϕ_1, ϕ_2 and obtain the third-order parameter ϕ_3 from the relation equation: $\sum_i \phi_i = 1$.

1. Lattice Boltzmann equation for conservative phase-field equation

The comprehensive derivation of LBM for the conservative phase-field equation is offered in this section. The Discrete Boltzmann equation (DBE) for ternary flow can be represented as:

$$\left(\frac{\partial}{\partial t} + \boldsymbol{e}_\alpha \cdot \nabla\right) h_\alpha^i = -\frac{1}{\lambda_\phi}(h_\alpha^i - h_\alpha^{i,eq}) + \Gamma_\alpha(\boldsymbol{e}_\alpha - \boldsymbol{u}) \cdot \boldsymbol{S_i}, \tag{22}$$

where $i = 1, 2, 3$, h_α^i and $h_\alpha^{i,eq}$ represent the particle distribution function and equilibrium distribution function for i^{th} component order parameter. $\boldsymbol{e}_\alpha$ denotes the lattice velocity in $D2Q9$ lattice given as:

$$\boldsymbol{e}_\alpha = \begin{cases} (0,0)c, & \alpha = 0 \\ (\cos\theta_\alpha, \sin\theta_\alpha)c, & \theta_\alpha = (\alpha-1)\pi/2, \quad \alpha = 1,2,3,4 \\ \sqrt{2}(\cos\theta_\alpha, \sin\theta_\alpha)c, & \theta_\alpha = (\alpha-5)\pi/2 + \pi/4, \quad \alpha = 5,6,7,8 \end{cases}$$

where c represents the lattice velocity unit. λ_ϕ is the relaxation time relevant to the mobility $M = \lambda_\phi c_s^2$, $c_s = \frac{1}{\sqrt{3}}c$ is the speed of sound. The equilibrium distribution function $h_\alpha^{i,eq}$ takes

the form:

$$h_\alpha^{i,eq} = t_\alpha \phi_i \left[1 + \left(\frac{\boldsymbol{e}_\alpha \cdot \boldsymbol{u}}{c_s^2} + \frac{(\boldsymbol{e}_\alpha \cdot \boldsymbol{u})^2}{2c_s^4} - \frac{\boldsymbol{u} \cdot \boldsymbol{u}}{2c_s^2} \right) \right]. \tag{23}$$

t_α is the weight with the value: $t_0 = 4/9, t_1 = t_3 = t_5 = t_7 = 1/9$ and $t_2 = t_4 = t_6 = t_8 = 1/36$. Γ_α can be calculated as $\Gamma_\alpha = h_\alpha^{i,eq}/\phi_i$. $\boldsymbol{S_i}$ is the source term from the governing equation. The macroscopic equation recovered by Chapman-Enskog expansion is then:

$$\frac{\partial \phi_i}{\partial t} + \nabla \cdot (\phi_i \boldsymbol{u}) = \nabla \cdot M \left(\nabla \phi_i - \frac{4}{\delta} \frac{\nabla \phi_i}{|\nabla \phi_i|} \phi_i (1 - \phi_i) + \frac{\phi_i^2}{\sum_{j=1}^3 \phi_j^2} \sum_{j=1}^3 \frac{4}{\delta} \frac{\nabla \phi_j}{|\nabla \phi_j|} \phi_j (1 - \phi_j) \right). \tag{24}$$

where the source term $\boldsymbol{S_i}$ for component i can be expressed as:

$$\boldsymbol{S_i} = \frac{4}{\delta} \frac{\nabla \phi_i}{|\nabla \phi_i|} \phi_i (1 - \phi_i) - \frac{\phi_i^2}{\sum_{j=1}^3 \phi_j^2} \sum_{j=1}^3 \frac{4}{\delta} \frac{\nabla \phi_j}{|\nabla \phi_j|} \phi_j (1 - \phi_j). \tag{25}$$

The recovered phase-field equation is identical to the proposed phase-field equation Eq.21. Then, we start to solve Eq.22 for i component by the time integration in $[t, t + \delta t]$:

$$h_\alpha^i(\boldsymbol{x} + \delta t \boldsymbol{e}_\alpha, t + \delta t) - h_\alpha^i(\boldsymbol{x}, t) = - \int_t^{t+\delta t} \frac{h_\alpha^i - h_\alpha^{i,eq}}{\lambda_\phi} dt +$$

$$\int_t^{t+\delta t} \Gamma_\alpha(\boldsymbol{u})(\boldsymbol{e}_\alpha - \boldsymbol{u}) \cdot \boldsymbol{S}_i dt. \tag{26}$$

Using the trapezoidal rule, the time-discretized equation becomes:

$$h_\alpha^i(\boldsymbol{x} + \delta t \boldsymbol{e}_\alpha, t + \delta t) - h_\alpha^i(\boldsymbol{x}, t) = - \frac{h_\alpha^i - h_\alpha^{i,eq}}{2\tau_\phi}\Big|_t - \frac{h_\alpha^i - h_\alpha^{i,eq}}{2\tau_\phi}\Big|_{t+\delta t}$$

$$+ \frac{\delta t}{2} \left[\Gamma_\alpha(\boldsymbol{u}(\boldsymbol{e}_\alpha - \boldsymbol{u}) \cdot \boldsymbol{S}_i)\big|_t + \Gamma_\alpha(\boldsymbol{u})(\boldsymbol{e}_\alpha - \boldsymbol{u}) \cdot \boldsymbol{S}_i\big|_{t+\delta t} \right]. \tag{27}$$

Here $\tau_\phi = \lambda_\phi/\delta t$ is dimensionless relaxation time. We introduce the modified distribution function $\bar{h}^i(\boldsymbol{x}, t)$:

$$\bar{h}_\alpha^i(\boldsymbol{x}, t) = h_\alpha^i(\boldsymbol{x}, t) + \frac{1}{2\tau_\phi} \left(h_\alpha^i - h_\alpha^{i,eq} \right)\Big|_t - \frac{\delta t}{2} \Gamma_\alpha(\boldsymbol{u})(\boldsymbol{e}_\alpha - \boldsymbol{u}) \cdot \boldsymbol{S}_i\Big|_t. \tag{28}$$

The LBM with the modified distribution function for the phase-field equation can be written as:

$$\bar{h}^i_\alpha(\boldsymbol{x} + \boldsymbol{e}_\alpha \delta t, t + \delta t) - \bar{h}^i_\alpha(\boldsymbol{x}, t) = -\frac{1}{\tau_\phi + 0.5}(\bar{h}^i_\alpha(\boldsymbol{x}, t) - \bar{h}^{i,eq}_\alpha)$$
$$+ \delta t \Gamma_\alpha(\boldsymbol{u})(\boldsymbol{e}_\alpha - \boldsymbol{u}) \cdot \boldsymbol{S}_i. \quad (29)$$

The equilibrium modified distribution function can be calculated by:

$$\bar{h}^{i,eq}_\alpha = h^{i,eq}_\alpha - \frac{\delta t}{2}\Gamma_\alpha(\boldsymbol{u})(\boldsymbol{e}_\alpha - \boldsymbol{u}) \cdot \boldsymbol{S}_i. \quad (30)$$

2. velocity-pressure based Lattice Boltzmann equation

The velocity-based Lattice Boltzmann equation for high density and viscosity contrasts is proposed in [35]. It is then applied to the conservative phase-field method [39, 40]. In our simulation, we use a velocity-pressure-based LBM, in which the distribution function is modified to recover the pressure [9].

The DBE for the velocity-pressure formulation is given as:

$$\left(\frac{\partial}{\partial t} + \boldsymbol{e}_\alpha \cdot \nabla\right) g_\alpha = -\frac{1}{\lambda}(g_\alpha - g^{eq}_\alpha) + F_\alpha. \quad (31)$$

The Chapman-Enskog expansion based on this DBE is given in Appendix A. The governing equations, Eq.19 and Eq.20, can be recovered from the DBE Eq.31. Following the same procedure of phase-field LBM derivation, The velocity-pressure based LBM is then given as:

$$\bar{g}_\alpha(\boldsymbol{x} + \boldsymbol{e}_\alpha \delta t, t + \delta t) - \bar{g}_\alpha(\boldsymbol{x}, t) = -\frac{1}{\tau_\rho + 0.5}(\bar{g}_\alpha(\boldsymbol{x}, t) - \bar{g}^{eq}_\alpha) + \delta t F_\alpha, \quad (32)$$

where τ_ρ is the dimensionless relaxation time, and $\bar{g}^{eq}_\alpha$ is the modified distribution function:

$$\bar{g}^{eq}_\alpha = g^{eq}_\alpha - \frac{1}{2}F_\alpha, \quad (33)$$

$$g^{eq}_\alpha = t_\alpha \bar{p} + \Gamma_\alpha c_s^2 - t_\alpha c_s^2, \quad (34)$$

where P represents the dynamic pressure and ρ represents the local density. $\bar{p}$ can be

calculated as $\bar{p} = \frac{P}{\rho}$. The source term of Eq.30 is composed of a collection of forcing terms:

$$F_\alpha = -\Gamma_\alpha(\boldsymbol{e}_\alpha - \boldsymbol{u}) \cdot \left(\frac{1}{\rho}\nabla P\right) + \Gamma(0)(\boldsymbol{e}_\alpha - \boldsymbol{u}) \cdot (\nabla\bar{p}) +$$

$$\Gamma_\alpha(\boldsymbol{e}_\alpha - \boldsymbol{u}) \cdot \left[\frac{\nu}{\rho}(\nabla\boldsymbol{u} + \nabla\boldsymbol{u}^T)\nabla\rho + \frac{1}{\rho}\boldsymbol{F}_s + \frac{1}{\rho}\boldsymbol{F}_b\right]. \quad (35)$$

$\boldsymbol{F}_s$ and $\boldsymbol{F}_b$ represent the surface tension force and the body force. The CSF formulation, Eq.16, is applied in our approach. Here we only consider the gravitational force as the body force which:

$$\boldsymbol{F}_b = (\rho - \rho_l)\boldsymbol{g}, \quad (36)$$

where $\boldsymbol{g}$ is the gravitation acceleration. ρ, ρ_l represents the local fluid density and the background liquid density. The derivatives of macroscopic value which appear in Eq.35 can be calculated by second order isotropic finite difference method [14]:

$$\frac{\partial\phi}{\partial x_i} = \sum_{\alpha\neq 0} \frac{t_\alpha\boldsymbol{e}_\alpha \cdot \hat{\boldsymbol{i}}[\phi(\boldsymbol{x} + \boldsymbol{e}_\alpha\delta t) - \phi(\boldsymbol{x} - \boldsymbol{e}_\alpha\delta t)]}{2c_s^2\delta t}. \quad (37)$$

Then $\nabla\rho$ can be calculated from $\nabla\phi$ which:

$$\nabla\rho = \sum_{i=1}^{3} \rho_i\nabla\phi_i. \quad (38)$$

After the collision and the propagation, we need to update the macroscopic value and parameters in the distribution function. We first update different order parameters by the particle distribution function of the order parameter $\bar{h}_\alpha^i$:

$$\phi_i = \sum_{\alpha=0}^{8} \bar{h}_\alpha^i. \quad (39)$$

The density is then updated from a linear interpolation function of the order parameters:

$$\rho = \sum_{i=1}^{3} \rho_i\phi_i. \quad (40)$$

As the same manner, the local viscosity and the relaxation time for distribution function g_α

can be updated as:

$$\nu = \sum_{i=1}^{3} \nu_i \phi_i, \tag{41}$$

$$\tau_\rho = \frac{\nu}{c_s^2 \delta t}. \tag{42}$$

The macroscopic values such as pressure and velocity can then be calculated from the zero and the first moment of the particle distribution function $\bar{g}_\alpha$:

$$\bar{p} = \sum_\alpha \bar{g}_\alpha + \frac{\delta t}{2} \sum_\alpha F_\alpha, \tag{43}$$

$$\boldsymbol{u} = \sum_\alpha \frac{\bar{g}_\alpha}{c_s^2} \boldsymbol{e}_\alpha + \frac{\delta t}{2c_s^2} \sum_\alpha F_\alpha \boldsymbol{e}_\alpha. \tag{44}$$

III.   NUMERICAL TESTS

The primary parameters that appear in simulations are the diameter of a bubble or a droplet, D, the dynamic viscosity of the ith component, η_i, and the surface tension between the ith and j^{th} components, σ_{ij}. They are used to calculate the dimensionless groups, which are summarized as follows:

$$Cn = \frac{\delta}{D},$$

$$La_{ij} = \frac{\sigma_{ij} \rho_i D}{\eta_i^2},$$

$$Bo_{ij} = \frac{|\rho_i - \rho_j| g D^2}{\sigma_{ij}},$$

$$Ar_i = \frac{\rho_i \sqrt{g D^3}}{\eta_i},$$

$$Oh_{ij} = \frac{\eta_i}{\sqrt{\rho_i \sigma_{ij} D}},$$

where δ is the interface thickness between two fluids, Cn, the Cahn number, which is defined as the ratio of the nonphysical interface thickness and the diameter. It is mostly used to evaluate if the phase-field method achieves a sharp interface limit by convergence test. La denotes the Laplace number which estimates the surface tension and momentum effect.

12

Bo and *Ar* are referred to as the Bond number (also known as Eötvös number) and the Archimedes number, respectively. These two parameters are introduced to monitor the dynamics of a rising bubble under the gravity field [41, 42]. The Ohnesorge number, *Oh*, is a measure of the strength of the interaction between the bubble and droplet. For an inertia regime, we have $Oh \ll 1$, when the fluids are brought into contact, there will be a significant fluid-fluid interaction at the interface region. When $Oh \gg 1$, the interaction will be smoothed by the fluids' viscosity. The spreading factor for the kth component can be calculated from the surface tensions, for example, $S_k = \sigma_{ij} - (\sigma_{ik} + \sigma_{jk})$. Partially engulfed, double emulsion and separate terminal morphology can be expected when we have a relative combination of spreading factors.

A. Parasitic Currents

The first test case we considered is a stationary droplet inside a liquid pool. A stationary droplet is placed in the middle of a quiescent fluid without a gravity field, and ideally, the velocity magnitude is expected to remain zero. However, due to the numerical error and the unbalanced pressure that occurs when the surface force comes into the system, the nonphysical parasitic currents appear at the interface region in the simulation [43]. As a result, knowing how to apply this surface force is critical to simulating multi-phase flow. For this test, we aim to distinguish different types of surface tension formulations that have been proposed previously and examine their performance under different system parameters. Initially, the droplet with $D/\Delta x = 50$ is centered in a square domain $L/D = 2$ with a fixed density and viscosity ratio $\rho* = \rho_1/\rho_2 = 1$, $\eta^* = \eta_1/\eta_2 = 1$, where subscript 1 represents the droplet and subscript 2 represents the background fluid. Four separate boundaries are subjected to the symmetric boundary condition. The relaxation times for the momentum equation and the phase-field equation are set as constant: $\tau_\rho = 0.5$ and $\tau_\phi = 0.3$, and the surface tension between two fluids is given as $\sigma_{12} = 1 \times 10^{-4}$ in lattice unit. A convergence test is carried out for different Cn for which we expect a lower intensity of parasitic currents when we gradually increase Cn. To make the system achieves an equilibrium state, the simulation results are reported after $T/t_0 = 200$, where $t_0 = \eta_1 D/2\sigma_{12}$ denotes the viscous time scale.

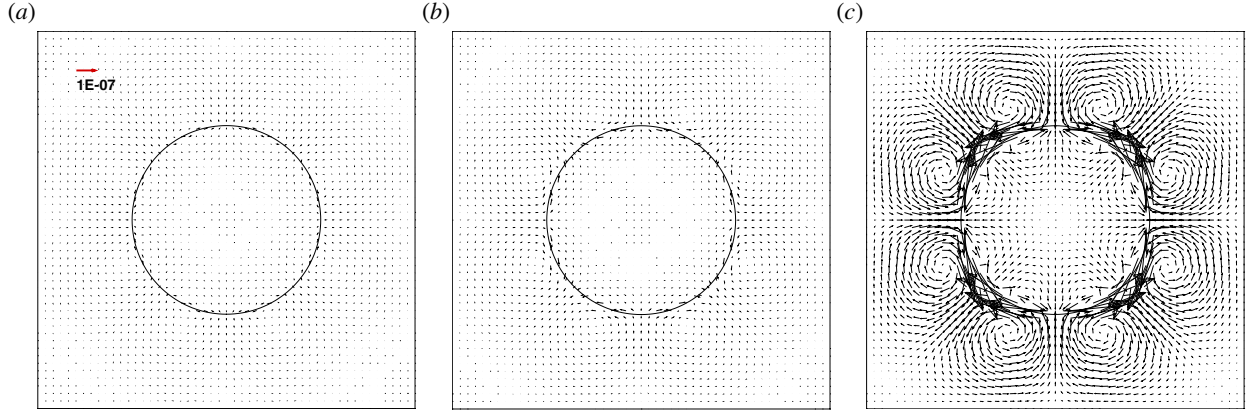To group different cases, the interface thicknesses are set as $\delta/\Delta x = [2, 3, 4]$, correspond-

FIG. 1: Parasitic currents' vectors in the single droplet simulation at $T = 200t_0$ by using (a) the continuous surface formulation, (b) the potential formulation, and (c) the stress formulation for $Cn = 0.08$. The interface is represented by a contour level $\phi = 0.5$. The reference vector with magnitude 1×10^{-7} is indicated by a red arrow in (a).

TABLE I: Convergence test of the parasitic currents' intensity with different Cn.

δ	Cn	$\boldsymbol{u}^2_{max}$ CSF	Potential form	Stress form
2	0.04	2.6×10^{-14}	2.0×10^{-11}	5.9×10^{-13}
3	0.06	2.3×10^{-15}	4.8×10^{-14}	1.4×10^{-13}
4	0.08	4.4×10^{-16}	1.6×10^{-15}	3.2×10^{-14}

ingly $Cn = [0.04, 0.06, 0.08]$. Figure 1 shows the flow field velocity vector when applying different formulations with $Cn = 0.08$. We provide the intensity of parasitic currents defined as $\boldsymbol{u}^2_{max}$ in Table I. According to Table I, the CSF formulation obtains a lower parasitic currents' intensity than the potential form formulation when we have a smaller interface thickness. All three formulations are able to reduce the parasitic currents' intensity as Cn increases.

We then simulate parasitic currents with fixed $Cn = 0.06$ and changing $La_{12} = [0.25 - 16]$. The results are posted in Table II. According to the simulation results, the parasitic currents'

TABLE II: Convergence test of the parasitic currents' intensity with different La.

La_{12}	$\boldsymbol{u}^2_{max}$ CSF	Potential form	Stress form
16	8.5×10^{-14}	1.1×10^{-12}	3.8×10^{-12}
4	2.2×10^{-14}	3.2×10^{-13}	1.1×10^{-12}
1	5.3×10^{-15}	1.1×10^{-13}	4.3×10^{-13}
0.25	2.4×10^{-15}	5.1×10^{-14}	1.8×10^{-13}

14

TABLE III: Convergence test of the parasitic currents' intensity based on coupled momentum equation and conservative phase-field equation with different La.

La_{12}	$\boldsymbol{u}^2_{max}$ CSF	Potential form	Stress form
16	5.0×10^{-12}	8.0×10^{-12}	1.2×10^{-10}
4	4.5×10^{-12}	5.4×10^{-12}	3.1×10^{-11}
1	3.9×10^{-12}	4.1×10^{-12}	8.7×10^{-12}
0.25	2.9×10^{-12}	2.7×10^{-12}	3.5×10^{-12}

intensity for all three different formulations has a decreasing trend when La_{12} is decreasing. When $La_{12} = 16$, the CSF formulation obtains a smaller parasitic currents' intensity than the other two formulations.

When coupled with the conservative phase-field equation, the effect of the combination of momentum and phase-field equations is presented. As well, we keep a fixed $Cn = 0.06$ and conduct the convergence test with changing $La_{12} = [0.25 - 16]$. Here, the density and viscosity ratio join $\rho^* = \rho_l/\rho_g = 10$, $\eta^* = \eta_l/\eta_g = 10$. According to Table III, the CSF and potential form formulations gain smaller parasitic currents' intensity than the stress form formulation when there is a large surface tension effect. If the surface tension between two fluids is small enough, the difference between the three formations can be neglected.

Through the results of only solving the momentum equation, we notice that if the shape of the droplet stays fixed and the system is under a large surface tension effect, the CSF formulation gains a small parasitic currents' intensity. When the momentum equation and the conservative phase-field equation are coupled, the parasitic currents' intensity of all three formulations increases. The reason is that the shape of the equilibrium droplet differs from the initial profile, and parasitic currents will evolve until there is a balance. Instead of the conservative phase-field equation, if the C-H equation and the potential form formulation are employed to simulate the interface interaction, they can decrease the parasitic currents' intensity by evolving the droplet to obtain minimum free energy. However, when the conservative phase-field equation is applied to the interface information, the curvature-driven term is subtracted from the chemical potential, which induces a different mechanism from the C-H equation. Among the three formations, the CSF formation is the only formulation that explicitly computes the curvature term and curvature-driven velocity which makes it consistent when coupling the conservative phase-field method.
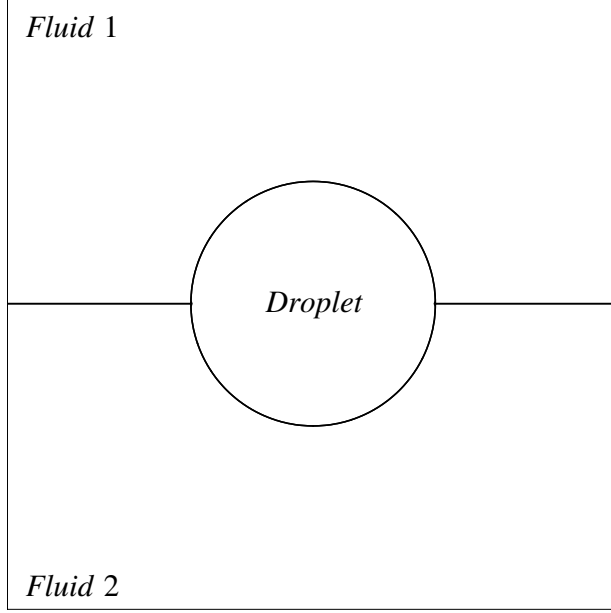
FIG. 2: Initial profile of the liquid lens simulation. A circle-shaped droplet is placed between two other fluids. The interface between different fluids is shown by $\phi = 0.5$.

B.   Liquid Lens

The liquid lens problem is widely applied as a validation case for ternary flow simulation, and we present this test to show our model's capability to deal with ternary flows. The initial state is shown as Fig. 2, where the droplet is placed into two fluids. The center of the droplet is settled in the middle of the square domain. This droplet keeps deforming due to the surface force and is resisted by viscous dissipation until it reaches equilibrium. By controlling the surface tension ratios, we could achieve different contact angles at triple contact points when the system reaches equilibrium. The initial order parameter profiles are set as the functions [22]:

$$
\begin{aligned}
\phi_2(\boldsymbol{x}, 0) &= \frac{1}{2} + \frac{1}{2} \tanh\left(\frac{2}{\delta} \min(|\boldsymbol{x} - \boldsymbol{x}_c| - R, y - y_c)\right), \\
\phi_3(\boldsymbol{x}, 0) &= \frac{1}{2} - \frac{1}{2} \tanh\left(\frac{2}{\delta} \max(-|\boldsymbol{x} - \boldsymbol{x}_c| + R, y - y_c)\right), \\
\phi_1(\boldsymbol{x}, 0) &= 1 - \phi_1(\boldsymbol{x}, 0) - \phi_2(\boldsymbol{x}, 0),
\end{aligned}
\tag{45}
$$

where $\boldsymbol{x}_c$ is the center of the liquid lens. Here, ϕ_1 represents the order parameter for the droplet, ϕ_2 and ϕ_3 represent the order parameters of the background Fluid 1 and Fluid 2. The basic theory of liquid lens can be expressed as Neumann's triangle. According to

16

Neumann's theory, when the whole system reaches an equilibrium state, the relation between contact angles θ_i, θ_j, θ_k and surface tensions of three phases σ_{ij}, σ_{ik}, σ_{jk} are given as:

$$\frac{\sin \theta_i}{\sigma_{jk}} = \frac{\sin \theta_j}{\sigma_{ik}} = \frac{\sin \theta_k}{\sigma_{ij}}, \tag{46}$$

The analytic contact angle can be calculated by:

$$\theta_i = \cos^{-1} \left(-\frac{\sigma_{ij}^2 + \sigma_{ik}^2 + \sigma_{jk}^2}{2\sigma_{ij}\sigma_{ik}} \right). \tag{47}$$

The method of the contact angle calculation from the simulation can be found in Appendix B, by which we can compare our results with analytic solutions. We start with the given surface tension ratios $(\sigma_{12}, \sigma_{13}, \sigma_{23}) \times 10^3 = (1, 1, 0.8), (1, 1, 1), (1, 1, 1.2), (1, 1, 1.4)$ and the equilibrium profiles of the liquid lens are shown in Fig. 3, where $\sigma^* = \sigma_{23}/\sigma_{12}$.
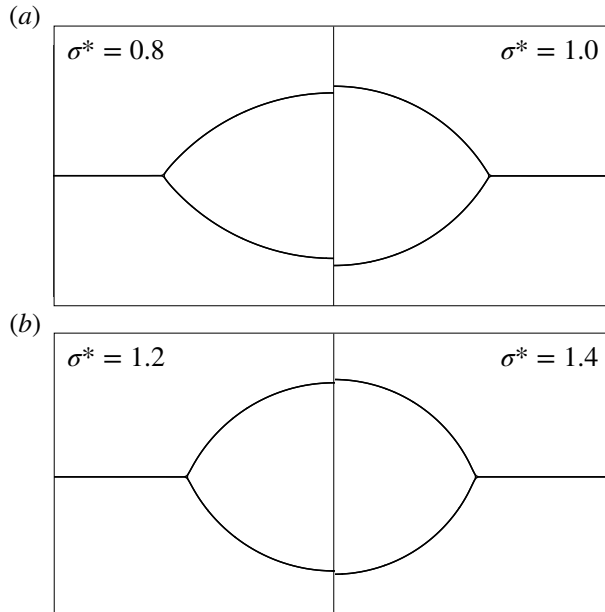
FIG. 3: Equilibrium morphology of the liquid lens simulations for various surface tensions between droplet and fluids with $Cn = 0.01875$: (a) (left panel) $\sigma^* = 0.8$; (right panel) $\sigma^* = 1.0$; (b) (left panel) $\sigma^* = 1.2$; (right panel) $\sigma^* = 1.4$.

The liquid lens length d which is the distance between two triple contact points for the equilibrium state is used to evaluate the accuracy of simulation methods. The analytic solution of d is:
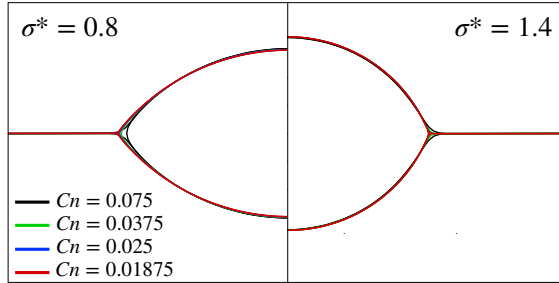
FIG. 4: Convergence test for contact lines with (left panel) $\sigma^* = 0.8$ and (right panel) $\sigma^* = 1.4$, $Cn = [0.01875 - 0.075]$. The contours of $\phi_i = 0.5$ for same Cn are indicated in a same color.

TABLE IV: The analytic solutions versus the simulation results for liquid lens length.

$D/\Delta x$	40	80	120	160	analytic solution
$\sigma^* = 0.8$	0.57493	0.59372	0.59954	0.60387	0.6128
$\sigma^* = 1.0$	0.53994	0.54804	0.55047	0.55192	0.5540
$\sigma^* = 1.2$	0.51734	0.52111	0.52185	0.52149	0.5220
$\sigma^* = 1.4$	0.50192	0.50289	0.50273	0.50220	0.5014

$$\frac{1}{d^2} = \frac{1}{8A}\left(\frac{2(\pi - \theta_1) - \sin(2(\pi - \theta_1)))}{\sin^2(\pi - \theta_1)} + \frac{2(\pi - \theta_3) - \sin(2(\pi - \theta_3)))}{\sin^2(\pi - \theta_3)}\right), \quad (48)$$

where $A = \pi R^2$ is the area of the initial droplet. Table IV shows the ratio of the liquid lens length to the domain length d/L with different diameters. We consider the viscosity and the density ratios ratio as $\eta_1/\eta_2 = \eta_1/\eta_3 = 1$, $\rho_1/\rho_2 = \rho_1/\rho_3 = 1$. The relaxation times are set as $\tau_\rho = 0.5, \tau_\phi = 3$.

Fig. 4 presents the convergence result for $\sigma^* = 0.8$ and $\sigma^* = 1.4$. The detailed results are provided in Table IV. In this case, we fix the interface thickness $\delta/\Delta x = 4$ and gradually increase the resolution. The simulation results converge to a better value toward the analytic solution as we decrease $Cn = 0.1 - 0.025$.

C. Droplet Morphology

In this simulation, as Fig. 5, we place two equal-sized droplets where $D/\Delta x = 40$ into square domain $L/D = 2.5$. Due to the difference in surface forces between those two droplets, we arrive at different results in terms of final morphology. When defining various fluid spreading phenomena, we use the spreading factor S. According to Pannacci [6], for
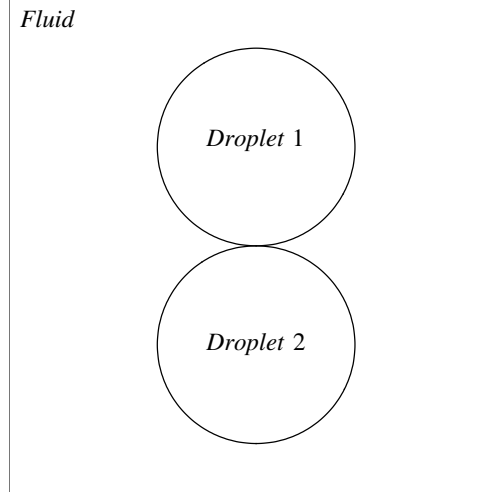
FIG. 5: Setup of the double emulsion simulation. Two equal-sized droplets are initially placed inside the background fluid. The center distance between two droplets is
$$C_d = D + \delta.$$

TABLE V: Parameters diagram of double emulsion simulations. Region (I-A) and region (I-B) indicate complete engulfment morphology, Region (II) represents separated morphology, and region (III) represents partially engulfed morphology.

Case Number	σ_{gb}	σ_{br}/σ_{gb}	σ_{gr}/σ_{gb}	S_b	S_g	S_r
I-A(1)	0.05	0.5	1.55	> 0	< 0	< 0
I-A(2)	0.05	1	2.05	> 0	< 0	< 0
I-B(1)	0.05	1.55	0.5	< 0	> 0	< 0
I-B(2)	0.05	2.05	1	< 0	> 0	< 0
II	0.05	0.35	0.35	< 0	< 0	> 0
III(1)	0.05	1	1	< 0	< 0	< 0
III(2)	0.05	0.5	1	< 0	< 0	< 0
III(3)	0.05	1	0.5	< 0	< 0	< 0
III(4)	0.05	1	1.5	< 0	< 0	< 0
III(5)	0.05	1.5	1	< 0	< 0	< 0
III(6)	0.0001	100	100	< 0	< 0	< 0

late-time morphology of two contact droplets, the complete engulfing (double emulsion) morphology appears while $S_b > 0, S_g < 0, S_r < 0$ or $S_g > 0, S_b < 0, S_r < 0$ corresponding to (I-A) region and (I-B) region. In (II) region, $S_r > 0, S_b < 0, S_g < 0$, the two droplets will break up into two parts. In (III) region, $S_r < 0, S_b < 0, S_g < 0$, the two droplets are partially engulfed by each other. Especially when we have a large surface tension ratio, Janus droplets will appear. In this case, the subscript g represents the green droplet, b denotes the blue droplet, and r is the red background fluid.

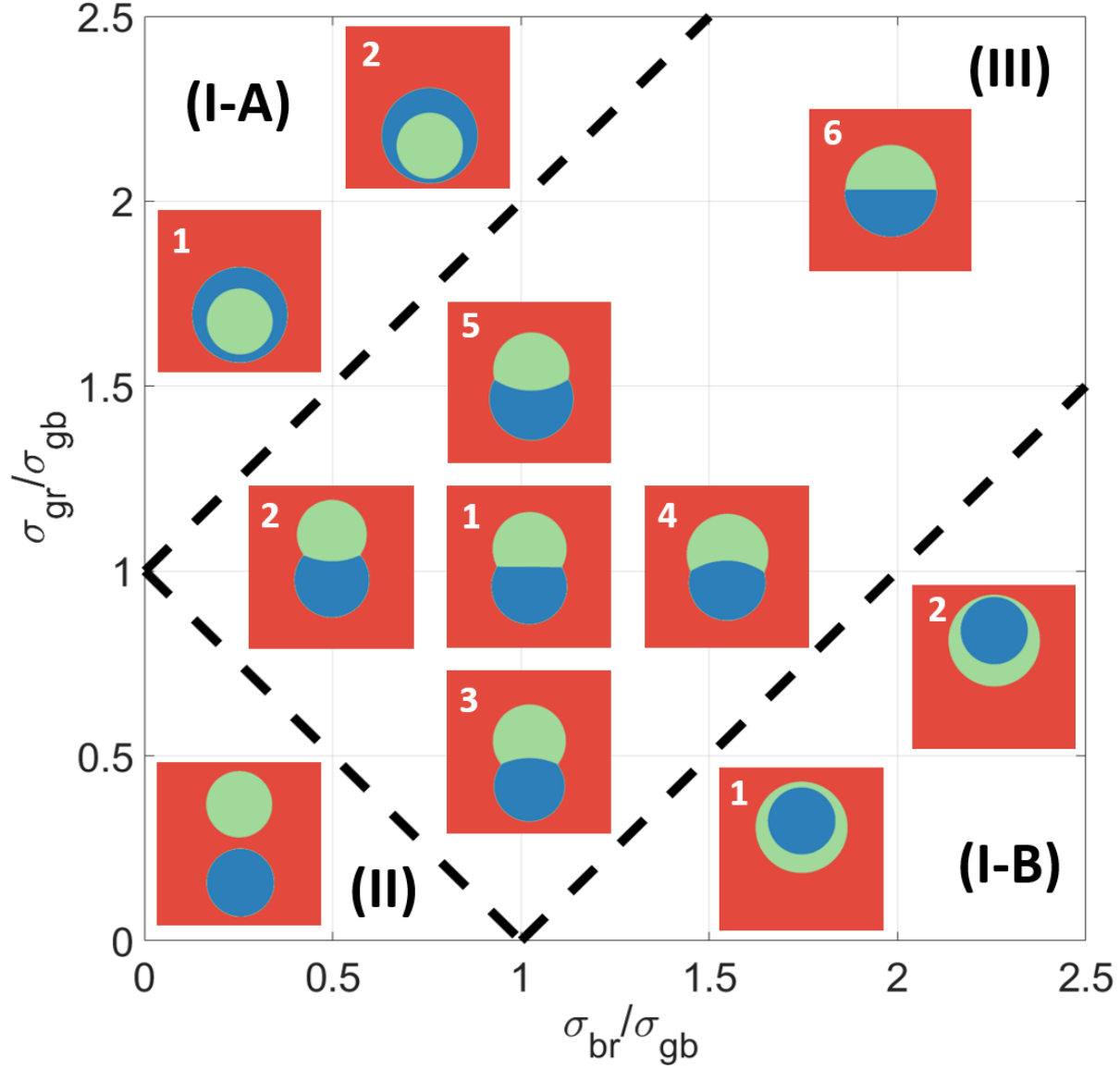In this series of simulations, we keep the surface tension between two droplets constant

FIG. 6: Morphology diagram of the terminal shapes for double emulsion simulation. (I-A), (I-B) present the double emulsion region, (II) shows the separate morphology region, (III) represents the partially engulfed region.

$\sigma_{gb} = 0.05$. The density and viscosity of different components are given as $\rho_r/\rho_g = \rho_r/\rho_b = 1, \mu_r/\mu_g = \mu_r/\mu_b = 1$. The relaxation times are $\tau_\rho = 0.1$ and $\tau_\phi = 0.3$. Morphology diagram Fig. 6 and Table V show our simulation results of a wide range of surface tension ratios. In Fig. 6, region (I) is composed of double emulsion final morphology. (I-A) and (I-B) separately shows the double emulsion with different outer components due to the spreading factors' difference. Region (II) presents a separate morphology, for which even with a contacting profile initially, two droplets will move in contrary directions. Region (III) is composed

of partially engulfed morphology. The liquid lens or Janus aggregate will appear for the equilibrium system. These results are consistent with previous simulation work [44].

D. Single rising bubble example

The single rising bubble process involves the rising bubble dynamics and bubble deformation which are basic problems of many industrial applications such as bubble column reactors and bitumen extraction. Several researchers have investigated the two-phase rising bubble problem before [4, 5, 45]. For this problem, we aim to compare our scheme with previous research by the benchmark problem that was studied in [45]. We initialize a bubble at the bottom of the domain and consider the density ratio $\rho_l/\rho_b = 10$, where the subscript l denotes the background fluid and b represents the bubble, the viscosity ratio $\eta_l/\eta_b = 10$, $Bo_{bl} = 10$ and $Ar_b = 35$. We place the bubble with diameters $D/\Delta x = 40, 80, 160$, and Cn can be calculated respectively as $Cn = [0.05, 0.025, 0.0125]$. The rectangular domain is given as $L \times 2L$, where $L/D = 2$. Initially, the center of the droplet is placed at (D, D).

Fig. 7(a) shows the evolution of the rising bubble shapes for $T/t_0 = [0 - 3]$ where $Cn = 0.0125$. Fig. 7(b) presents the convergence test of the rising bubbles' morphology with different Cn. The bubble shapes of different cases converge as we decrease Cn or increase the number of grid points. We can then find the temporal development of the mass center of the bubble, $C_m = \sum 4\phi_b y/\pi D^2$ where ϕ_b denotes the order parameter for the bubble, and y is the vertical displacement of the bubble according to the axis, and also the scaled average velocity V from Fig. 8 (a) and (b). Both results are compared with FeatFlow with a grid spacing of $1/320$ [45]. The comparison shows that our simulation results converge nicely and are in good agreement with the FeatFlow solution.

IV.   INTERACTION OF A RISING BUBBLE AND A STATIONARY DROPLET

Based on the single bubble rising test, we set up a ternary flow system to simulate the dynamics of the rising bubble and droplet interaction. The major application of this problem in the industry can be found in froth flotation [1, 3]. The froth flotation extracts the minerals from the slurry with the assistance of water foam or air bubbles. We model the coalescence and deformation of an air bubble and an oil droplet by imposing a gravitational
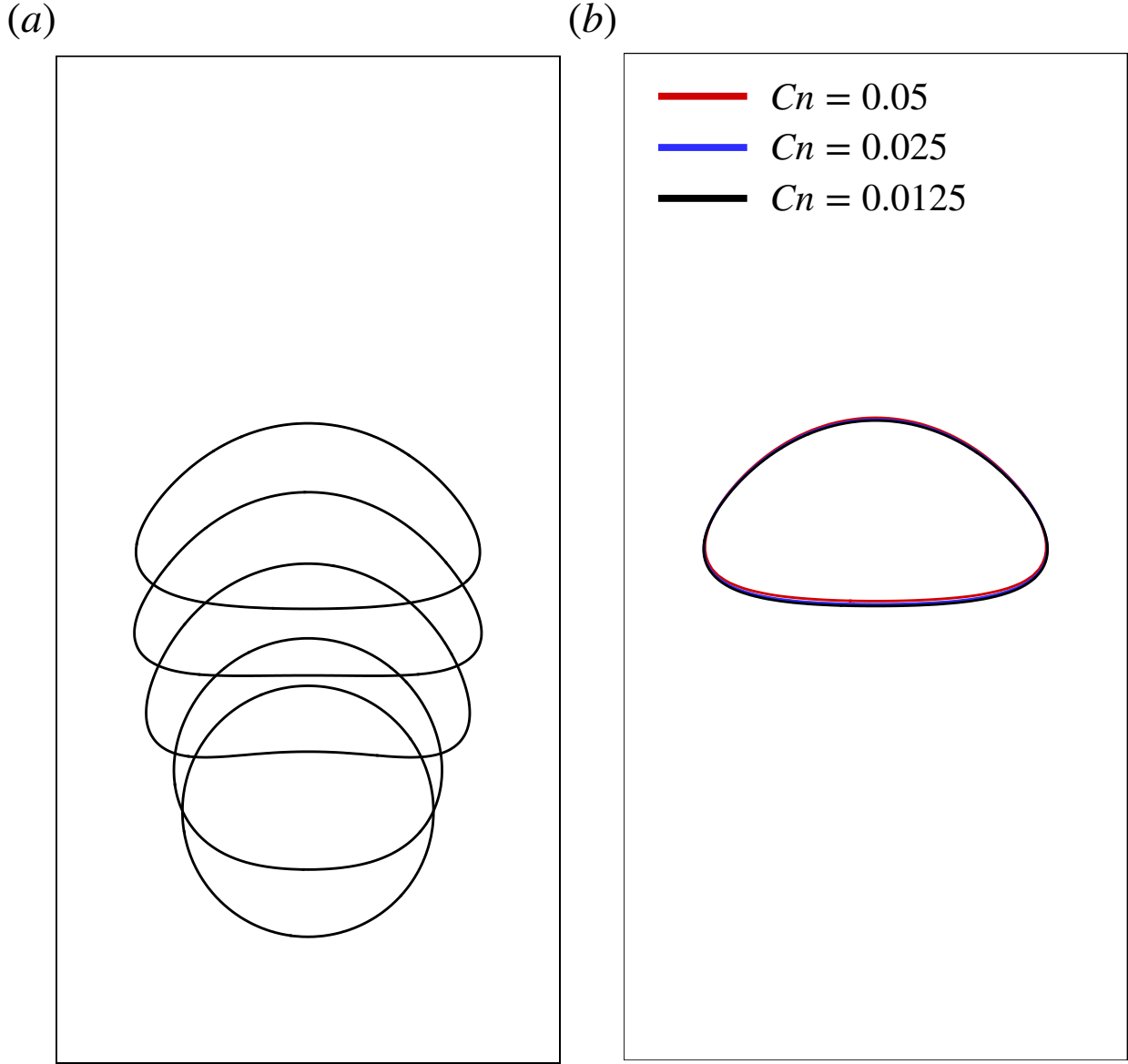
FIG. 7: (a) Evolution of rising bubble shapes for $T/t_0 = [0 - 3]$, where time is scaled by $t_0 = \sqrt{2D/g}$, with $Bo_{bl} = 10, Ar_b = 35$. (b) Convergence test of the bubble shape with $Cn = [0.05, 0.025, 0.0125]$ at $T/t_0 = 3$

.

force. To understand this process, the rising dynamics and morphology change of different size bubbles and oil droplets are needed to be considered. The previous works based on froth flotation concentrate more on the bubble-droplet aggregate forming and ideal cases which include only slow speed and small-size bubbles. We here investigate a larger-size bubble and droplet interaction for which we increase $Bo_{bl} = [1 - 8]$ and test different spreading factors
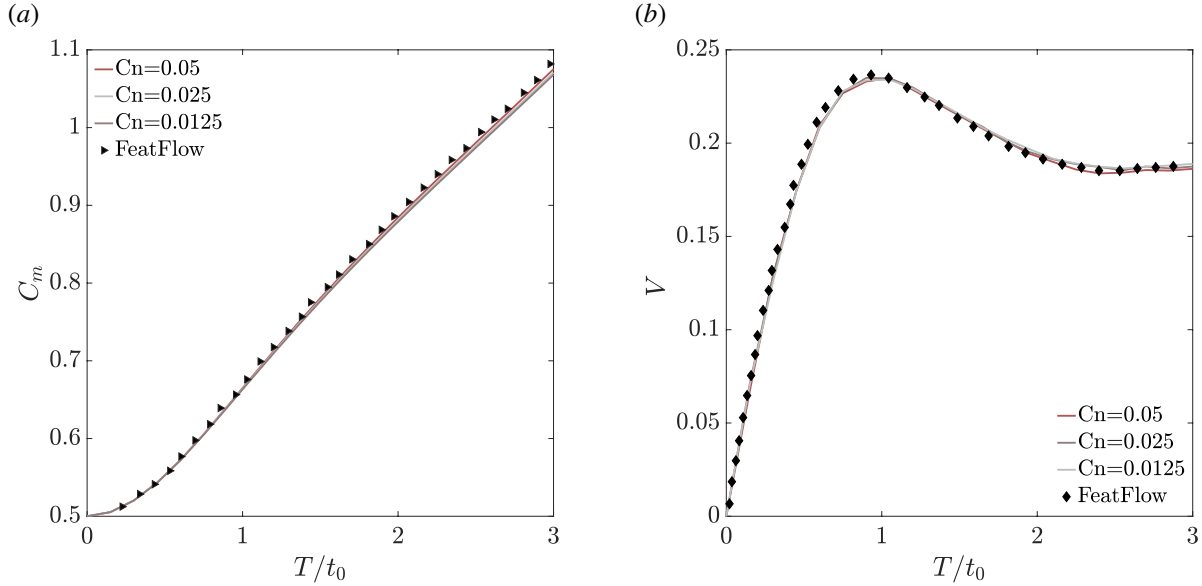
FIG. 8: Convergence test of the temporal development of the (a)mass center of the bubble C_m and (b) average rising velocity V which is scaled by $v_0 = \sqrt{2gD}$ with $Cn = [0.0125, 0.025, 0.05]$. When $Cn < 0.0375$, the rising velocity and the mass center nearly converge to the same value.

TABLE VI: Parameters diagram of ternary flow rising bubble simulation.

Bo	Ar	Oh (Double emulsion)	Oh (Partially engulfed)
1	8	0.06	0.13
2	8	0.09	0.18
3	8	0.11	0.22
4	8	0.13	0.25
5	8	0.14	0.28
6	8	0.15	0.31
7	8	0.17	0.33
8	8	0.18	0.35

that provide different perspectives on this process.

In a ternary flow, the rising bubble with a lower density will progressively climb to the top and collide with the oil droplet, which has a density similar to the background fluid. Refer to Fig. 6, when two droplets contact each other under distinct spreading factors, we can expect different final morphology. Besides, the surface tension and the viscosity of different components will also affect the interaction dynamics. In this case, Bo_{bl} and Ar_b are used to characterize the rising process, and we employ $Oh_{dl} = \frac{\eta_d}{\sqrt{\rho_d \sigma_{dl} D_0}}$ to evaluate the intensity of the interaction. Here, ρ_d is the droplet density, σ_{dl} denotes the surface tension between
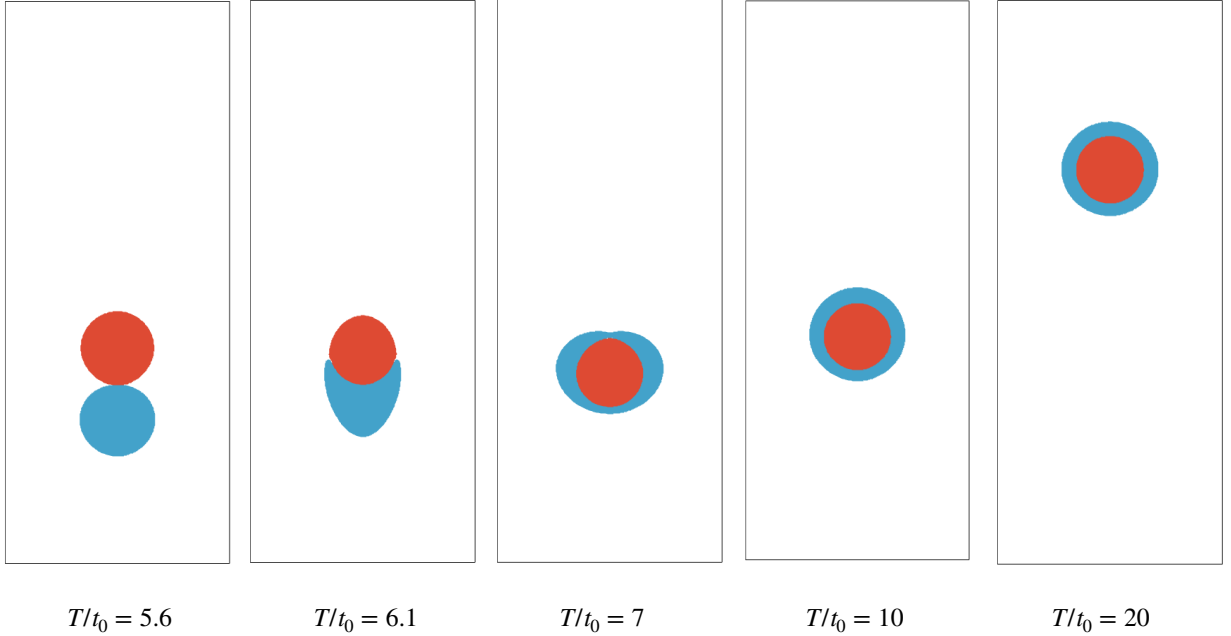
FIG. 9: Evolution of the aggregate for $T/t_0 = [5.6 - 20]$, when the surface tension or spreading factors satisfy the condition of the double emulsion morphology under $Bo_{bl} = 1$. The red oil droplet will be fully engulfed by the rising blue bubble at $T/t_0 \approx 7$.

the droplet and background liquid, D_0 is the diameter of the droplet, and η_d represents the viscosity of the droplet. During the simulation, we keep track of the entire dynamic process by the average rising velocity $V_d = v/\sqrt{gD_0}$ and the center of the mass C_m. The time scale now is modified to $t_0 = \sqrt{D_0/g}$. We would like to divide the whole rising process into three stages: (1) the bubble rises first in a gravitational field; (2) the bubble makes contact with the top droplet, initiating the interaction; and (3) the aggregate rises to the top with a terminal velocity in the final stage.

For the simulation, the diameter of two equal-sized droplets is $D/\Delta x = 48$, and the centers are placed at $(20/3, 1) \times D, (20/3, 3) \times D$. The density ratio and viscosity ratio are set as $\rho_d/\rho_b = 100, \rho_d/\rho_l = 1, \eta_d/\eta_b = 100$, and $\eta_d/\eta_l = 1$. The interface thickness is given as $\delta/\Delta x = 4$. The full-way bounce-back no-slip boundary condition is applied to the top and bottom boundaries, while the symmetric boundary condition is applied to the left and right boundaries [13].

Table VI lists Bo_{bl}, Ar_b and Oh_{dl} for testing cases. We keep $Ar_b = 8$, and gradually increase Bo_{bl}. Both partially engulfed morphology and double emulsion morphology are tested. It is noted that we neglect the case of the second double emulsion morphology
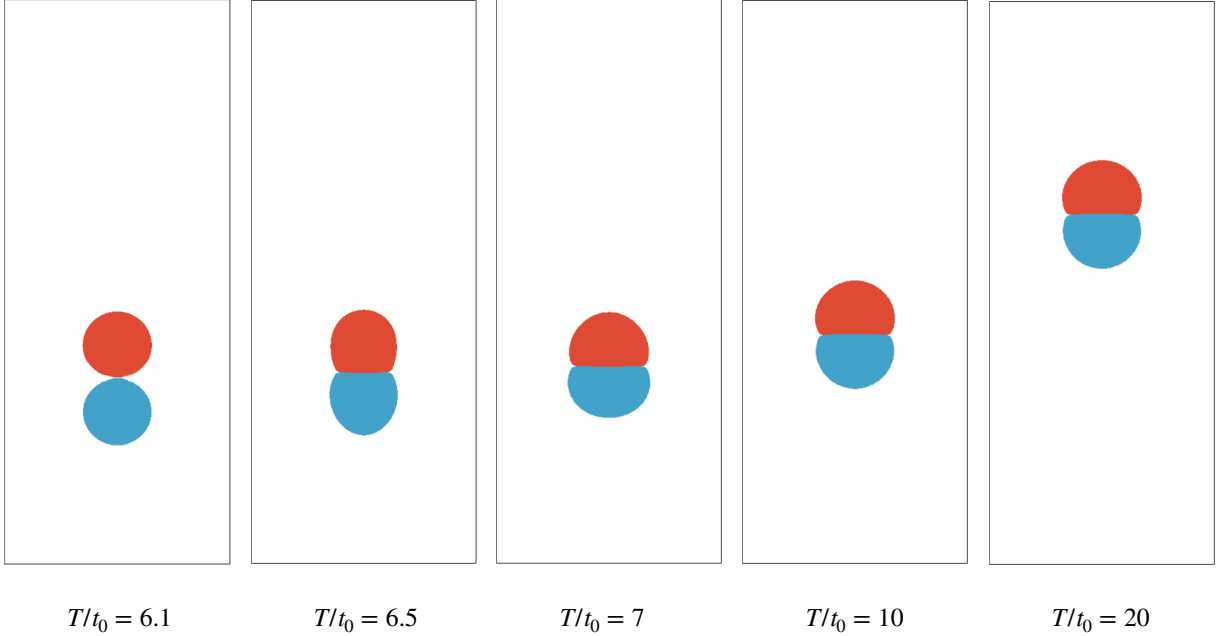
24

FIG. 10: Evolution of the aggregate for $T/t_0 = [6.1 - 20]$, when the surface tension or spreading factors satisfy the condition of the partially engulfed morphology under $Bo_{bl} = 1$. After the blue bubble contacts the red oil droplet, they will maintain this partially engulfed morphology steady, and gradually move to the top.

where $S_d > 0$. When $S_d > 0$, a stable terminal morphology only exists when $Bo_{bl} \ll 1$, which makes the entire rising process inefficient. The time evolution of the rising bubble for different morphological situations with $Bo_{bl} = 1$ is shown in Fig. 9 and Fig. 10. Fig. 12 and Fig. 14 present the rising velocity and the center position of the bubble for partially engulfed morphology and double emulsion morphology. In Fig. 13 and Fig. 15, we show the droplet's rising velocity and center position.

We first discuss the case in which the rising bubble will try to partially engulf the oil droplet under this surface tension ratio. As shown in Fig. 12, Fig. 13 the cases with small Bo_{bl} and Oh_{dl} approach the contact point faster than the cases with large Bo_{bl} and Oh_{dl}. For the inertia regime, $Oh_{dl} \ll 1$, the surface tension force induces a quick contacting or engulfing process for which the viscous resistance hardly affects the dynamics. Under this situation, there is a severe interaction and a short period of engulfment once the rising bubble touches the oil droplet. However, following the interaction, the droplet under a smaller Bo_{bl} obtains a bigger terminal velocity for the aggregate and continues to rise. It is the morphology that affects the system. Situations with large Bo_{bl} show a velocity decline
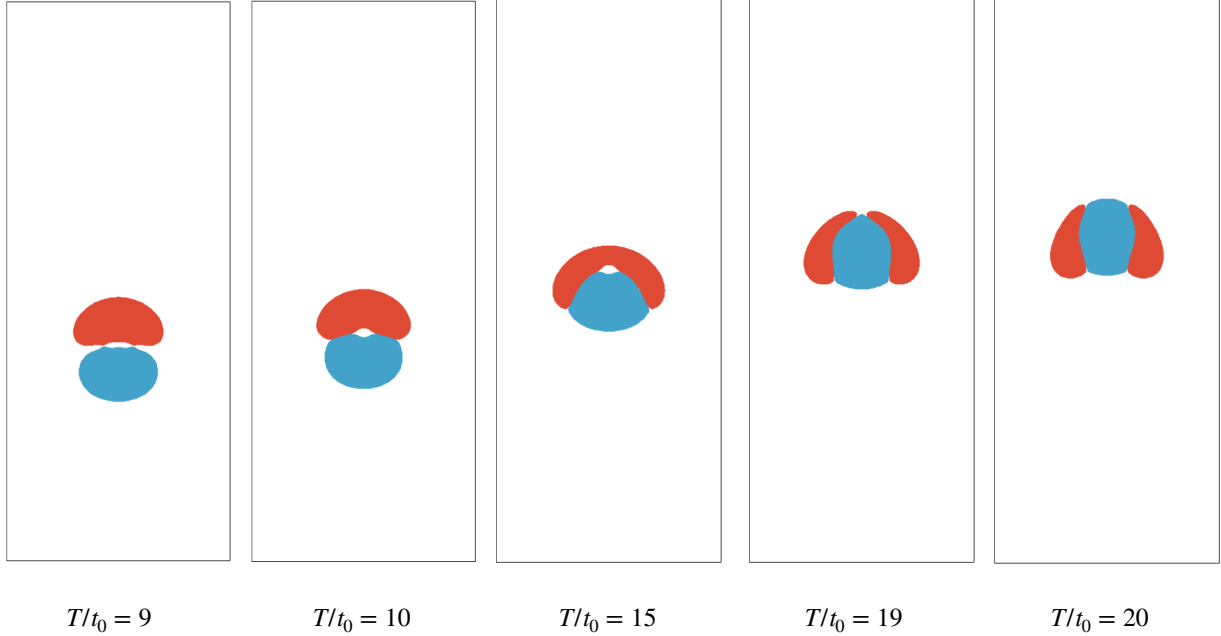
25

FIG. 11: Evolution of the aggregate for $T/t_0 = [9 - 20]$, when the surface tension or spreading factors satisfy the condition of the partially engulfed morphology under $Bo_{bl} = 8$. After the blue bubble contacts the red oil droplet, they first form this partially engulfed morphology. Due to the large rising speed of the aggregate, the oil droplet will break but stick to the rising bubble.

due to the droplet's distortion. Since, compared to gravity, the surface force is still too weak to maintain the shape of this aggregate or partially engulfed morphology, the top droplet splits into two parts for $Bo_{bl} = 8$, as seen in Fig. 11. Fig. 12 and Fig. 13 indicate that when $Bo_{bl} = 8$, the rising bubble will continue to rise and keep the droplet aside. In conclusion, the center of the droplet exhibits a clear trend, as is the case when a small Bo_{bl} rises faster during the process.

For double emulsion cases, the initial acceleration and the terminal velocity are quite similar under different Bo_{bl}. From Table VI, we notice that Oh_{dl} for double emulsion is smaller compared to partially engulfed cases. That accounts for why the rising aggregate with double emulsion morphology can maintain this shape unchanged. The surface tension is able to keep the morphology from deforming further, resulting in a comparable drag force. While the cases with small Oh decelerate during the interaction stage, the aggregate of bubble and droplet will keep an even smaller deformation during the rising process compared to large Bo_{bl} cases.
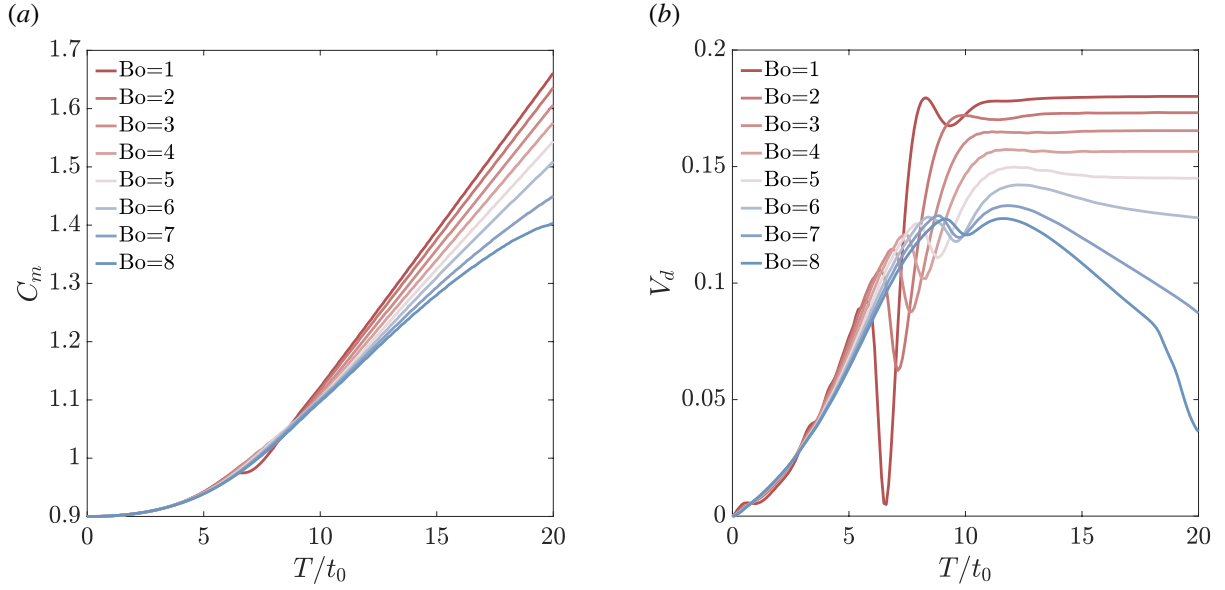
26

FIG. 12: Dynamics of the rising bubble and droplet interaction with partially engulfed morphology. (a) Mass center of the oil droplet C_m development with $Bo_{bl} = [1-8]$. (b) Scaled average rising velocity V_d of the droplet.
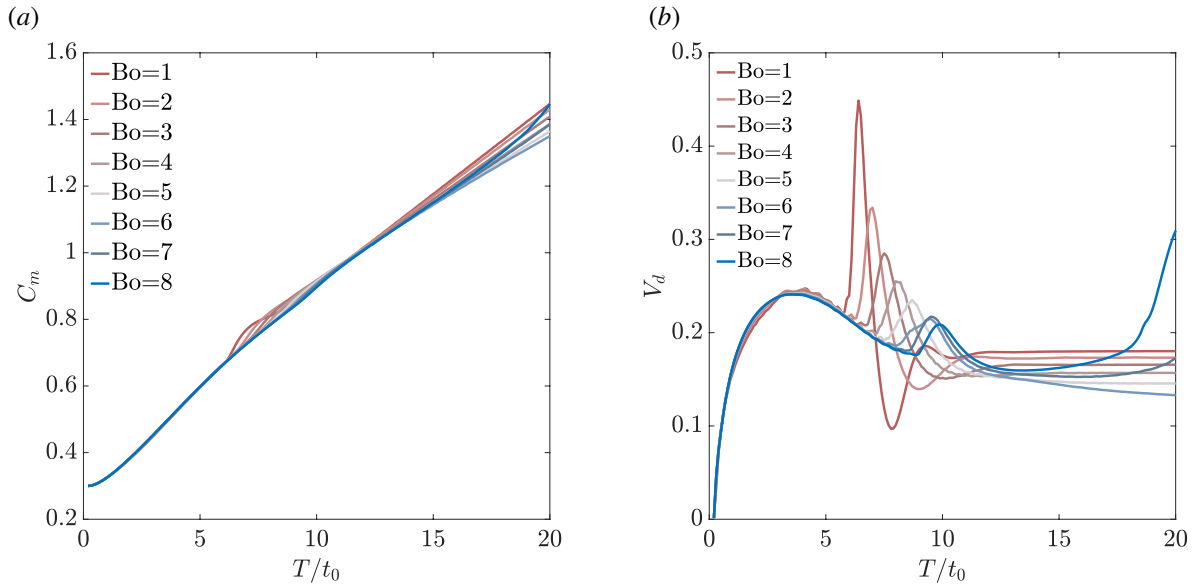

FIG. 13: Dynamics of the rising bubble and droplet interaction with partially engulfed morphology. (a) Mass center of the bubble C_m development with $Bo_{bl} = [1-8]$. (b) Scaled average rising velocity V_d of the bubble.

According to our simulation results of $Bo_{bl} = [1-8]$, the bubble with a small Bo_{bl} which implies a relatively smaller diameter in reality, maintains its shape and rises fast in both double emulsion and partially engulfed morphology. The rising velocity, dominated by
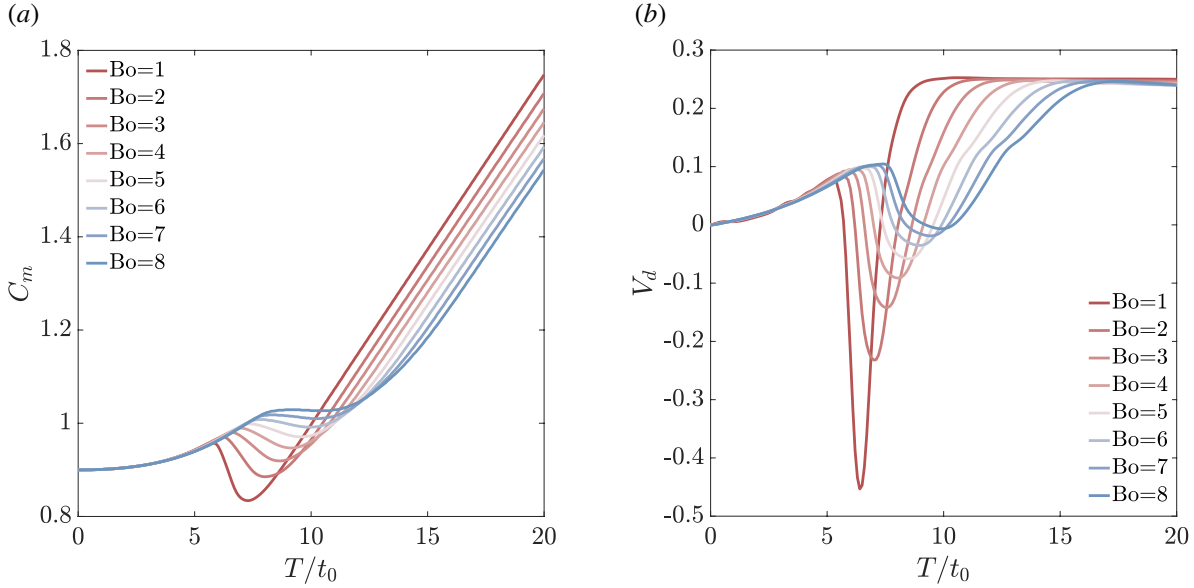
27

FIG. 14: Dynamics of the rising bubble and droplet interaction with double emulsion morphology. (a) Mass center of the oil droplet C_m development with $Bo_{bl} = [1-8]$. (b) Scaled average rising velocity V_d of the droplet.
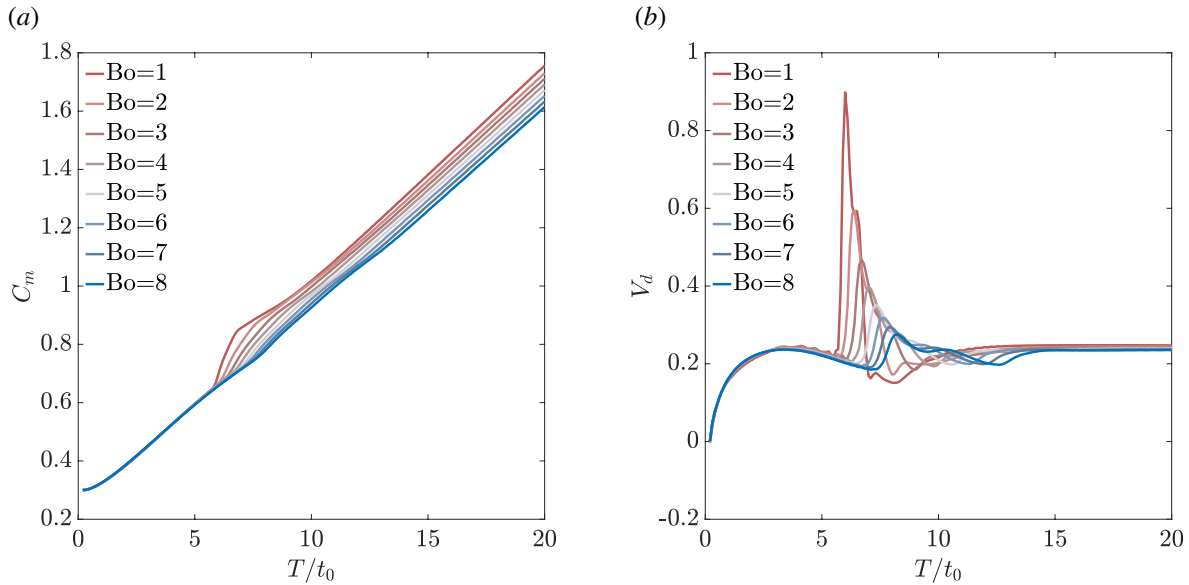

FIG. 15: Dynamics of the rising bubble and droplet interaction with double emulsion morphology. (a) Mass center of the bubble C_m development with $Bo_{bl} = [1-8]$. (b) Scaled average rising velocity V_d of the bubble.

gravity, is affected by surface force until the completion of the interaction process. However, the intensity of the interaction does not affect the rising process too much, the aggregate stability does. Although we expect a quicker rising velocity when Bo_{bl} are small, the stable

double emulsion morphology keeps different-sized bubbles at the same terminal velocity. Among the partially engulfed morphology cases, the drag force breaks up the aggregate and highly influences the rising speed.

In this simulation, we aim to learn an entire ideal rising process which includes the process of the bubble rising, the interaction between the static droplet and the rising bubble, as well as the rising of the aggregate, for the larger size oil, $R \sim 1mm$ in two dimensions (2D). The difference between the droplet dynamics in 2D and 3D simulations has been investigated previously [46–48]. For this problem, we admit that 2D simulations might differ from 3D simulations regarding the terminal velocity value and the interaction process. However, As shown in Fig. 6, the equilibrium morphology of the contacting of two droplets only depends on the spreading factor. It is also proved by 3D simulations and experiments [49]. Thus, the final morphology in 2D and 3D simulations should be highly consistent. In addition, We agree that the 2D and 3D simulations are different for modeling contact line dynamics. Nevertheless, the aggregate's terminal velocity is greatly influenced by the final morphology, but not the intensity of the interactions. In this case, the difference in interaction process or contact line dynamics will not affect the final rising velocity.

V. CONCLUDING REMARKS

In this article, we presented the simulation work on a rising bubble and a droplet interaction. The conservative phase-field equation was applied as the interface capturing method, and the order parameters were calculated by Lattice Boltzmann equations. In addition, the hydrodynamic properties were calculated by the velocity-pressure-based Lattice Boltzmann equation, which recovers the pressure evolution equation and the momentum equation. As for surface force formulation, rather than using the potential form formulation, we utilize the CSF formulation to keep consistency. Based on convergence tests for both solving the single momentum equation and the coupled momentum phase-field equation, we argue the CSF formulation can simulate relatively small parasitic currents' intensity when curvature is fixed in the simulation. The liquid lens simulation assessed the conservative character and tested the accuracy of the recent method to solve ternary flow systems. We verify the current surface tension force applied in this system by the droplet morphology simulation, which provides the reference morphology under different spreading factors.

Based on the single rising bubble simulation, the bubble-droplet interaction in a ternary flow is presented. We learned that the final rising velocity of the bubble-droplet aggregate highly depends on the morphology stability when $Bo_{bl} = [1-8]$. We compared the interaction time and the final velocity for various morphology cases. A smaller Bo_{bl} and Oh_{dl} resulted in a faster interaction process with a higher interaction intensity. We also detected a higher terminal velocity with a smaller Bo_{bl} for the partially engulfed morphology. Due to slight distortion, the cases of double emulsion morphology achieved a similar terminal velocity among different Bo_{bl}.

ACKNOWLEDGEMENT

Appendix A: Chapman Enskog Analysis

In this section, we present a Chapman-Enskog analysis based on the Discrete Boltzmann equation. We start with the Discrete Boltzmann equation given as Eq.29:

$$\frac{\partial g_\alpha}{\partial t} + \boldsymbol{e}_\alpha \cdot \nabla g_\alpha = -\frac{g_\alpha - g^{eq}}{\lambda} + F_\alpha. \tag{A1}$$

When we consider δt to be the small parameter, the fundamental expansions based on δt for the distribution function and the time derivative are expressed as follows:

$$g_\alpha(\boldsymbol{x}, t) = g_\alpha^{eq}(\boldsymbol{x}, t) + \delta t g_\alpha^{(1)}(\boldsymbol{x}, t) + \delta t^2 g_\alpha^{(2)}(\boldsymbol{x}, t), \tag{A2}$$

$$\partial_t = \partial_{t0} + \delta t \partial_{t1}. \tag{A3}$$

The leading order equation of δt is then calculated as:

$$\frac{\partial g_\alpha^{eq}}{\partial t_0} = \frac{g_\alpha^{(1)}}{\tau} + F_\alpha, \tag{A4}$$

and the δt^2 order equation can be expressed as:

$$\frac{\partial g_\alpha^{eq}}{\partial t_1} + (\partial_{t0} + \boldsymbol{e}_\alpha \cdot \nabla)g_\alpha^{(1)} = \frac{g_\alpha^{(2)}}{\tau}. \tag{A5}$$

We add those two equations together and cut off the high-order terms. We will obtain:

$$\frac{\partial g_\alpha^{eq}}{\partial t} + \boldsymbol{e}_\alpha \cdot \nabla g_\alpha^{eq} + \delta t(\partial_{t0} + \boldsymbol{e}_\alpha \cdot \nabla)g_\alpha^{(1)} = -\frac{1}{\lambda}(g_\alpha - g_\alpha^{eq}) + F_\alpha. \tag{A6}$$

To design the target governing equations given as Eq. 19, Eq. 20, the following moments of the equilibrium distribution have to be restricted:

$$\sum_\alpha g_\alpha^{eq} = \bar{p}, \tag{A7}$$

$$\sum_\alpha g_\alpha^{eq} \boldsymbol{e}_\alpha = \boldsymbol{u}c_s^2, \tag{A8}$$

31

$$\sum_\alpha g_\alpha^{eq} \boldsymbol{e}_\alpha \boldsymbol{e}_\alpha = \boldsymbol{u}\boldsymbol{u}c_s^2 + \bar{p}c_s^2. \tag{A9}$$

Besides, the moments of the forcing term can be also derived from the momentum equation Eq. 20:

$$\sum_\alpha F_\alpha = -\boldsymbol{u} \cdot \nabla \bar{p}, \tag{A10}$$

$$\sum_\alpha F_\alpha \boldsymbol{e}_\alpha = \frac{c_s^2}{\rho}\left(-\nabla P + \rho\nabla\bar{p} + \nu(\nabla\boldsymbol{u} + \nabla\boldsymbol{u}^T)\nabla\rho + \boldsymbol{F}_s + \boldsymbol{F}_b\right), \tag{A11}$$

$$\sum_\alpha F_\alpha \boldsymbol{e}_\alpha \boldsymbol{e}_\alpha = c_s^2 \boldsymbol{u} \cdot \nabla \bar{p}. \tag{A12}$$

Within the aforementioned preclusion, the following equations can be deduced from the zeroth and the first moments of Eq.A6 :

$$\frac{\partial \bar{p}}{\partial t} + \nabla \cdot \boldsymbol{u}c_s^2 + \boldsymbol{u} \cdot \nabla \bar{p} = 0 \tag{A13}$$

$$\frac{\partial \boldsymbol{u}}{\partial t} + \nabla \cdot \boldsymbol{u}\boldsymbol{u} + \frac{\delta t}{c_s^2}\nabla \cdot \Pi^{(1)} = -\frac{1}{\rho}\nabla P + \frac{\nu}{\rho}(\nabla\boldsymbol{u} + \nabla\boldsymbol{u}^T)\nabla\rho + \frac{F_s}{\rho} + \frac{F_b}{\rho} \tag{A14}$$

We notice that Eq. 13 is composed of the pressure evolution equation and the continuity equation, which can be shown as:

$$\frac{\partial P}{\partial t} - \rho c_s^2 \nabla \cdot \boldsymbol{u} + \boldsymbol{u} \cdot \nabla P = \bar{p}\left(\frac{D\rho}{Dt} + \rho\nabla \cdot \boldsymbol{u}\right) + P\nabla \cdot \boldsymbol{u} \approx 0. \tag{A15}$$

In Eq. 14, $\Pi^{(1)} = \tau\nabla \cdot \sum_\alpha g_\alpha^{eq}\boldsymbol{e}_\alpha\boldsymbol{e}_\alpha\boldsymbol{e}_\alpha$, when we consider the kinematic viscosity $\nu = \tau c_s^2 \delta t$, Eq.A14 becomes:

$$\frac{\partial \boldsymbol{u}}{\partial t} + \nabla \cdot \boldsymbol{u}\boldsymbol{u} = -\frac{1}{\rho}\nabla P + \frac{1}{\rho}\nabla \cdot \eta(\nabla\boldsymbol{u} + \nabla\boldsymbol{u}^T) + \frac{F_s}{\rho} + \frac{F_b}{\rho}, \tag{A16}$$

where $\eta = \nu\rho$ is the dynamic viscosity. In the final, the governing equations, Eq.A13 and Eq.A16 are retrieved from the Discrete Boltzmann equation A1. It is noticed that, by trapezoidal rule, the Discrete Boltzmann equation Eq.A1 can be further discretized into LBE Eq. 32. Through the Taylor-series expansion of the Eq. 32, it can recover Eq. 1 up to 2nd order of δt [29].

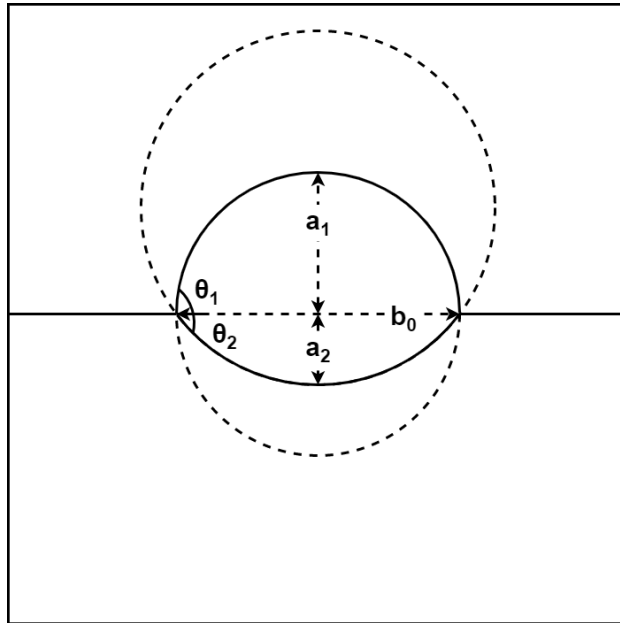## Appendix B: Contact angle calculation

FIG. 16: The schematic of spreading of a liquid lens.

In this section, we show the method for obtaining the contact angle from the liquid lens simulation. A stationary liquid lens schematic is shown in FIG.16, where the droplet achieves equilibrium between two background fluids. In this figure, b_0 is the length between two three-phase contact points. a_1 and a_2 are the distances between the droplet top and bottom and the two-phase contact line. b_0, a_1, a_2 can be obtained by the order parameter $\phi = 0.5$. the upper contact angle and lower contact angle θ_1 and θ_2 can then be calculated as: $\theta_i^{eq} = 180° - 2\arctan(\frac{b_0}{2a_i})$. Finally, we can calculate the contact angle as $\theta = \theta_1 + \theta_2$.

[1] R. Moosaiand R. A. Dawe, Gas attachment of oil droplets for gas flotation for oily wastewater cleanup, Separation and purification technology **33**, 303 (2003).

[2] J. Saththasivam, K. Loganathan, and S. Sarp, An overview of oil–water separation using gas flotation systems, Chemosphere **144**, 671 (2016).

[3] C. Grattoni, R. Moosai, and R. A. Dawe, Photographic observations showing spreading and non-spreading of oil on gas bubbles of relevance to gas flotation for oily wastewater cleanup, Colloids and Surfaces A: Physicochemical and Engineering Aspects **214**, 151 (2003).

[4] L. Amaya-Bowerand T. Lee, Single bubble rising dynamics for moderate reynolds number using lattice boltzmann method, Computers & Fluids **39**, 1191 (2010).

[5] L. Amaya-Bowerand T. Lee, Numerical simulation of single bubble rising in vertical and inclined square channel using lattice boltzmann method, Chemical Engineering Science **66**, 935 (2011).

[6] N. Pannacci, H. Bruus, D. Bartolo, I. Etchart, T. Lockhart, Y. Hennequin, H. Willaime, and P. Tabeling, Equilibrium and nonequilibrium states in microfluidic double emulsions, Physical review letters **101**, 164502 (2008).

[7] J. Guzowski, P. M. Korczyk, S. Jakiela, and P. Garstecki, The structure and stability of multiple micro-droplets, Soft Matter **8**, 7269 (2012).

[8] D. Jacqmin, An energy approach to the continuum surface tension method, in *34th Aerospace sciences meeting and exhibit* (1996) p. 858.

[9] L. Baroudiand T. Lee, Simulation of a bubble rising at high reynolds number with mass-conserving finite element lattice boltzmann method, Computers & Fluids **220**, 104883 (2021).

[10] J. W. Cahn, Free energy of a nonuniform system. ii. thermodynamic basis, The Journal of chemical physics **30**, 1121 (1959).

[11] S. M. Allenand J. W. Cahn, A microscopic theory for antiphase boundary motion and its application to antiphase domain coarsening, Acta metallurgica **27**, 1085 (1979).

[12] J. Kim, A continuous surface tension force formulation for diffuse-interface models, Journal of Computational Physics **204**, 784 (2005).

[13] T. Leeand L. Liu, Lattice boltzmann simulations of micron-scale drop impact on dry surfaces, Journal of Computational Physics **229**, 8045 (2010).

[14] T. Leeand C.-L. Lin, A stable discretization of the lattice boltzmann equation for simulation of incompressible two-phase flows at high density ratio, Journal of Computational Physics **206**, 16 (2005).

[15] R. H. H. Abadi, A. Fakhari, and M. H. Rahimian, Numerical simulation of three-component multiphase flows at high density and viscosity ratios using lattice boltzmann methods, Physical Review E **97**, 033312 (2018).

[16] Y. Sunand C. Beckermann, Sharp interface tracking using the phase-field equation, Journal of Computational Physics **220**, 626 (2007).

[17] P. Yue, C. Zhou, and J. J. Feng, Spontaneous shrinkage of drops and mass conservation in

phase-field simulations, Journal of Computational Physics **223**, 1 (2007).

[18] L. Zheng, T. Lee, Z. Guo, and D. Rumschitzki, Shrinkage of bubbles and drops in the lattice boltzmann equation method for nonideal gases, Physical Review E **89**, 033302 (2014).

[19] R. Folch, J. Casademunt, A. Hernández-Machado, and L. Ramírez-Piscina, Phase-field model for hele-shaw flows with arbitrary viscosity contrast. ii. numerical study, Physical Review E **60**, 1734 (1999).

[20] P.-H. Chiuand Y.-T. Lin, A conservative phase field method for solving incompressible two-phase flows, Journal of Computational Physics **230**, 185 (2011).

[21] M. Geier, A. Fakhari, and T. Lee, Conservative phase-field lattice boltzmann model for interface tracking equation, Physical Review E **91**, 063309 (2015).

[22] R. H. H. Abadi, M. H. Rahimian, and A. Fakhari, Conservative phase-field lattice-boltzmann model for ternary fluids, Journal of Computational Physics **374**, 668 (2018).

[23] S. Aihara, T. Takaki, and N. Takada, Multi-phase-field modeling using a conservative allen–cahn equation for multiphase flow, Computers & Fluids **178**, 141 (2019).

[24] L. Zheng, S. Zheng, and Q. Zhai, Multiphase flows of n immiscible incompressible fluids: Conservative allen-cahn equation and lattice boltzmann equation method, Physical Review E **101**, 013305 (2020).

[25] J. U. Brackbill, D. B. Kothe, and C. Zemach, A continuum method for modeling surface tension, Journal of computational physics **100**, 335 (1992).

[26] D. Jacqmin, Calculation of two-phase navier–stokes flows using phase-field modeling, Journal of Computational Physics **155**, 96 (1999).

[27] B. Lafaurie, C. Nardone, R. Scardovelli, S. Zaleski, and G. Zanetti, Modelling merging and fragmentation in multiphase flows with surfer, Journal of Computational Physics **113**, 134 (1994).

[28] T. Leeand P. F. Fischer, Eliminating parasitic currents in the lattice boltzmann equation method for nonideal gases, Physical Review E **74**, 046709 (2006).

[29] T. Leeand C.-L. Lin, An eulerian description of the streaming process in the lattice boltzmann equation, Journal of Computational Physics **185**, 445 (2003).

[30] T. Leeand C.-L. Lin, A characteristic galerkin method for discrete boltzmann equation, Journal of Computational Physics **171**, 336 (2001).

[31] X. Shanand H. Chen, Lattice boltzmann model for simulating flows with multiple phases and

components, Physical review E **47**, 1815 (1993).

[32] Q. Li, K. H. Luo, Q. Kang, Y. He, Q. Chen, and Q. Liu, Lattice boltzmann methods for multiphase flow and phase-change heat transfer, Progress in Energy and Combustion Science **52**, 62 (2016).

[33] T. Abadie, J. Aubin, and D. Legendre, On the combined effects of surface tension force calculation and interface advection on spurious currents within volume of fluid and level set frameworks, Journal of Computational Physics **297**, 611 (2015).

[34] T. Inamuro, T. Ogata, S. Tajima, and N. Konishi, A lattice boltzmann method for incompressible two-phase flows with large density differences, Journal of Computational physics **198**, 628 (2004).

[35] Y. Zuand S. He, Phase-field-based lattice boltzmann model for incompressible binary fluid systems with density and viscosity contrasts, Physical Review E **87**, 043301 (2013).

[36] J. Kim, Phase field computations for ternary fluid flows, Computer methods in applied mechanics and engineering **196**, 4779 (2007).

[37] H. G. Leeand J. Kim, An efficient numerical method for simulating multiphase flows using a diffuse interface model, Physica A: Statistical Mechanics and its Applications **423**, 33 (2015).

[38] T. Lee, Effects of incompressibility on the elimination of parasitic currents in the lattice boltzmann equation method for binary fluids, Computers & Mathematics with Applications **58**, 987 (2009).

[39] A. Fakhari, T. Mitchell, C. Leonardi, and D. Bolster, Improved locality of the phase-field lattice-boltzmann model for immiscible fluids at high density ratios, Physical Review E **96**, 053301 (2017).

[40] M. O. Abu-Al-Saud, S. Popinet, and H. A. Tchelepi, A conservative and well-balanced surface tension model, Journal of Computational Physics **371**, 896 (2018).

[41] H. Liang, Y. Li, J. Chen, and J. Xu, Axisymmetric lattice boltzmann model for multiphase flows with large density ratio, International Journal of Heat and Mass Transfer **130**, 1189 (2019).

[42] J. Huaand J. Lou, Numerical simulation of bubble rising in viscous liquid, Journal of Computational Physics **222**, 769 (2007).

[43] S. Popinet, Numerical models of surface tension, Annual Review of Fluid Mechanics **50**, 49 (2018).

[44] N. Wang, C. Semprebon, H. Liu, C. Zhang, and H. Kusumaatmaja, Modelling double emulsion formation in planar flow-focusing microchannels, Journal of Fluid Mechanics **895** (2020).

[45] S.-R. Hysing, S. Turek, D. Kuzmin, N. Parolini, E. Burman, S. Ganesan, and L. Tobiska, Quantitative benchmark computations of two-dimensional bubble dynamics, International Journal for Numerical Methods in Fluids **60**, 1259 (2009).

[46] H. Zhouand C. Pozrikidis, The flow of suspensions in channels: single files of drops, Physics of Fluids A: Fluid Dynamics **5**, 311 (1993).

[47] H. Tang, L. Wrobel, and Z. Fan, Tracking of immiscible interfaces in multiple-material mixing processes, Computational Materials Science **29**, 103 (2004).

[48] G. Soligo, A. Roccon, and A. Soldati, Coalescence of surfactant-laden drops by phase field method, Journal of Computational Physics **376**, 1292 (2019).

[49] S. B. Choi, J. Y. Park, J. Y. Moon, and J. S. Lee, Effect of interactions between multiple interfaces on the rheological characteristics of double emulsions, Physical Review E **97**, 062603 (2018).